A Framework for Design, Modeling, and Identification of Compliant Biomimetic Swimmers

by

Adam Joseph Wahab

Submitted to the Department of Mechanical Engineering
in partial fulfillment of the requirements for the degree of

Master of Science in Mechanical Engineering

at the

MASSACHUSETTS INSTITUTE OF TECHNOLOGY

September 2008

Author .....
Department of Mechanical Engineering
August 29, 2008

Certified by .....
Kamal Youcef-Toumi
Professor of Mechanical Engineering
Thesis Supervisor

Accepted by .....
Lallit Anand
Chairman, Department Committee on Graduate Students

A Framework for Design, Modeling, and Identification of Compliant Biomimetic Swimmers

by

Adam Joseph Wahab

Submitted to the Department of Mechanical Engineering
on August 29, 2008, in partial fulfillment of the
requirements for the degree of
Master of Science in Mechanical Engineering

Abstract

Research interests in fish-like devices are generally driven by the notion that through eons of evolution fish have developed optimal mechanisms for efficient propulsion and high degrees of maneuverability. Engineered fish-like devices have been developed in hope of mimicking the capabilities of their biological counterparts, but success has been marginal. This thesis considers a unique class of underactuated biomimetic swimmers with compliant bodies that swim by exploiting their structural dynamics. Practical matters surrounding the design and modeling of these swimmers are addressed and explicit references are made to fish morphology and swimming behaviours with the aim of linking biological and engineering design elements, a deficiency in existing literature. A hybrid modeling scheme is presented drawing upon conventional engineering primitives and experimental data. Both a hardware prototype swimmer and a unique motion capture system were developed to demonstrate the described methods. Experimental and simulated results are compared.

Thesis Supervisor: Kamal Youcef-Toumi

Title: Professor of Mechanical Engineering

Acknowledgments

I would like to thank my thesis supervisor, Professor Kamal Youcef-Toumi, for his advice and patience throughout the duration of this project.

Secondly, I wish to thank my labmates, Dan Burns and Vijay Shilpiekandula, for making me feel like part of the Mechatronics Research Lab from day one, and for having a sense of humour for days two through five-hundred and ninety-eight. Additionally, I would like to thank Pablo Valdivia y Alvarado for his advice regarding fabrication of the prototype swimmer.

Next, I would like to thank my colleague, Dan Klenk. Going above and beyond the duties of a UROP, his contributions spanned all facets of the prototype design and testing.

Most importantly, my heartfelt thanks goes to my parents, Randy and Maret, and to my brother and best friend, Matthew. I would not be where I am today without their devoted support and encouragement.

Contents

List of Figures

List of Tables

Acronyms

ABS	Acrylonitrile butadiene styrene
AUV	Autonomous underwater vehicle
BCF	Body and/or caudal fin
BL	Body length
CA	Cyanoacrylate
CCD	Charge-coupled device
DC	Direct current
DPIV	Digital particle image velocimetry
GPIO	General purpose input/output
IEEE	Institute of Electrical and Electronics Engineers
IR	Infrared
LE	Leading edge
LED	Light emitting diode
LVDT	Linear variable differential transformer
MEMS	Microelectromechanical systems
MPEG	Moving Pictures Experts Group
MPF	Median and/or paired fins
PTFE	Polytetrafluoroethylene
PWM	Pulse width modulation
ROV	Remotely operated vehicle
SMD	Surface-mount devices
TE	Trailing edge
TIFF	Tagged image file format
USB	Universal serial bus

Parameters and Units

Æ	Aspect ratio	
a	Slope of lift curve	rad^{-1}
α	Angle of attack	rad
$\boldsymbol{B}$	Buoyancy force vector	N
b	Tip-to-tip span of lifting surface	m, BL
β	Angle of sideslip	rad
C	Non-dimensional hydrodynamic coefficient	
c	Chord length	m, BL
D	Drag	N
E	Modulus of elasticity	N/m^2
η	Oswald efficiency factor	
g	Gravitational acceleration	m/s^2
H	Lateral displacement amplitude	m, BL
h	Lateral displacement	m, BL
$\mathbf{I}$	Inertias tensor	kg·m^2
I	Mass (or area) moment of inertia	kg·m^2 (or m^4)
K	Moment about ${}^b x$-axis	N·m
L	Lift	N
$\mathbf{L}$	Transformation matrix	
Λ	Sweep angle	$^\circ$
λ	Taper ratio	

(continued on next page)

(continued from previous page)

M	Moment about ${}^{b}y$-axis	N·m
m	Material mass	kg
$\widetilde{m}$	Added mass coefficient	kg
μ	Dynamic viscosity	kg/m·s
N	Moment about ${}^{b}z$-axis	N·m
ν	Kinematic viscosity	m^2/s
ω	Beat frequency	rad/s
$\boldsymbol{\omega}$	Angular velocity vector	rad/s
p	Velocity component about the ${}^{b}x$-axis	rad/s
$\boldsymbol{\phi}$	Attitude vector of Euler angles	°
q	Velocity component about the ${}^{b}y$-axis	rad/s
$\Re$	Set of all real numbers	
${}^{2}\mathbf{R}_{1}$	Rotation matrix transforming from frame 1 to frame 2	
Re	Reynolds number	
ρ	Density	kg/m^3
${}^{i}\boldsymbol{r}_{b}$	Position vector	m, BL
r	Velocity component about the ${}^{b}z$-axis	rad/s
S	Planform area	m^2
St	Strouhal number	
Θ	Pitch amplitude	°
t	Time	s
θ	Pitch angle	°

(continued on next page)

(continued from previous page)

u	Velocity component in the ${}^b x$-direction	m/s, BL/s
V	Volume	m^3
v	Velocity component in the ${}^b y$-direction	m/s, BL/s
$\boldsymbol{v}$	Velocity vector	m/s, BL/s
$\boldsymbol{W}$	Weight vector	N
w	Velocity component in the ${}^b z$-direction	m/s, BL/s
X	Force along ${}^b x$-direction	N
Y	Force along ${}^b y$-direction	N
Z	Force along ${}^b z$-direction	N

Subscripts and Superscripts

b	With respect to body-fixed reference frame or property of body
B	Pertaining to body center of buoyancy
c	With respect to observer- or camera-fixed reference frame
CF	Pertaining to the caudal fin
cs	Cross-sectional
f	Property of fluid medium
i	With respect to Earth-fixed inertial reference frame
m	Pertaining to the body center of mass
PF	Pertaining to the pectoral fins
r	Pertaining to the root of a lifting surface

(continued on next page)

(continued from previous page)

T	Pertaining to the tail (including the caudal fin)
TP	Pertaining to the tail plate
t	Pertaining to the tip of a lifting surface

Operators

$c_{(\cdot)}$	$\cos(\cdot)$
$s_{(\cdot)}$	$\sin(\cdot)$
ϵ_{jkl}	Levi-Civita operator
δ_{ab}	Kronecker delta
$\frac{D(\cdot)}{Dt}$	Material derivative
∂	Partial differential
$\langle\cdot\rangle$	Time average
$(\cdot)^{\mathsf{T}}$	Matrix transpose
$\|\cdot\|$	Vector magnitude
$\times$	Vector cross product
$\cdot$	Vector dot product
$\dot{(\,)}$	Derivative with respect to time

Chapter 1

Introduction

present a practical methodology for characterizing and modeling compliant fish-like devices that use flapping-foil propulsion. Non-invasive computer vision-based techniques were devised to estimate complex interactions between the compliant devices and their surrounding fluid medium. Efforts were made to maintain generality throughout the presented methods, allowing them to be readily adapted and expanded upon for use in design and control of similar devices. A prototype swimmer was constructed for both demonstration and validation purposes. To highlight accessibility, clever uses of inexpensive consumer-grade hardware in both the swimmer and motion-capture system are also described in detail. Throughout the text, references are made to fish morphology and swimming behaviours in an effort to emphasize links between biological and engineering design elements.

In this chapter, sources of motivation behind the development of biomimetic aquatic propulsors are provided followed by an overall summary of the body of work with

brief descriptions of the subsequent chapters.

1.1 Challenges in Biomimetic Swimmer Design

Despite the fact that most fluid environments are stochastic by nature, formulations for modeling the arbitrary motions of rigid bodies through fluid media are readily available in the literature [31], [32], [40], [50], [57]. For practical purposes, most of the difficulties in modeling nonlinear fluid-body interactions may be surmounted by using linearization techniques and empirical relationships, yielding more than acceptable results [13], [41].

Biomimetic devices utilizing fish-like propulsion diverge from the rigid tubular designs of conventional submersibles. Continually deforming articulated bodies complicate the fluid-structure interactions beyond the scope of rigid body models. Devices with infinite degrees of freedom, such as the compliant swimmers considered here, further complicate problem of modeling fluid-body interactions by introducing an additional set of nonlinear dynamics.

1.2 Objectives and Focus

Chapter 2 provides an introduction to relevant aspects of fish anatomy and swimming characteristics. A survey of previous related studies is presented, highlighting contributions and existing deficiencies.

Chapter 3 discusses the elements of the biomimetic swimmer model, drawing upon modeling techniques typically used for the engineering of aircraft and nautical vessels as well as models for less conventional flapping foil propulsion.

Chapter 4 details the development of a prototype compliant swimmer, its pilot control interface, and the vision-based data acquisition system used to record its swimming motions.

Chapter 5 describes the procedure used to extract kinematics from the recorded video frames and presents experimental results and compares the measured swimmer kinematics with simulated results generated by a numerical model.

Chapter 6 summarizes the thesis content and provides suggestions for future development and analysis of compliant biomimetic swimming devices.

The objectives of this thesis are to provide a structured basis for modeling, designing, and analyzing compliant fish-like swimmers using hybrid methodologies that draw upon both biological characteristics of fish and conventional engineering knowledge. The proposed framework aims to help minimize resources, emphasizing experiment time and cost, in developing and characterizing prototype swimmers.

Chapter 2

Background

In the following sections, fundamentals of fish biology and swimming are briefly discussed, followed by a review of literature and studies that are relevant to the modeling and design of biomimetic swimmers.

2.1 School of Fish

Before diving into a technical discussion of the design and modeling of fish-like swimmers, it is worth developing an appreciation of pertinent ichthyological* lexicon.

*Ichthyology is the zoological field devoted to studying fish.

2.1.1 Anatomy

Most fish share a number of common morphological characteristics, those of relevance to this work are indicated in Figure 2-1. While some terms are not unique to fish anatomy, they are included here for clarity. The terms dorsal, ventral, anterior, and posterior, refer to the body's back, underbelly, head and tail regions, respectively.

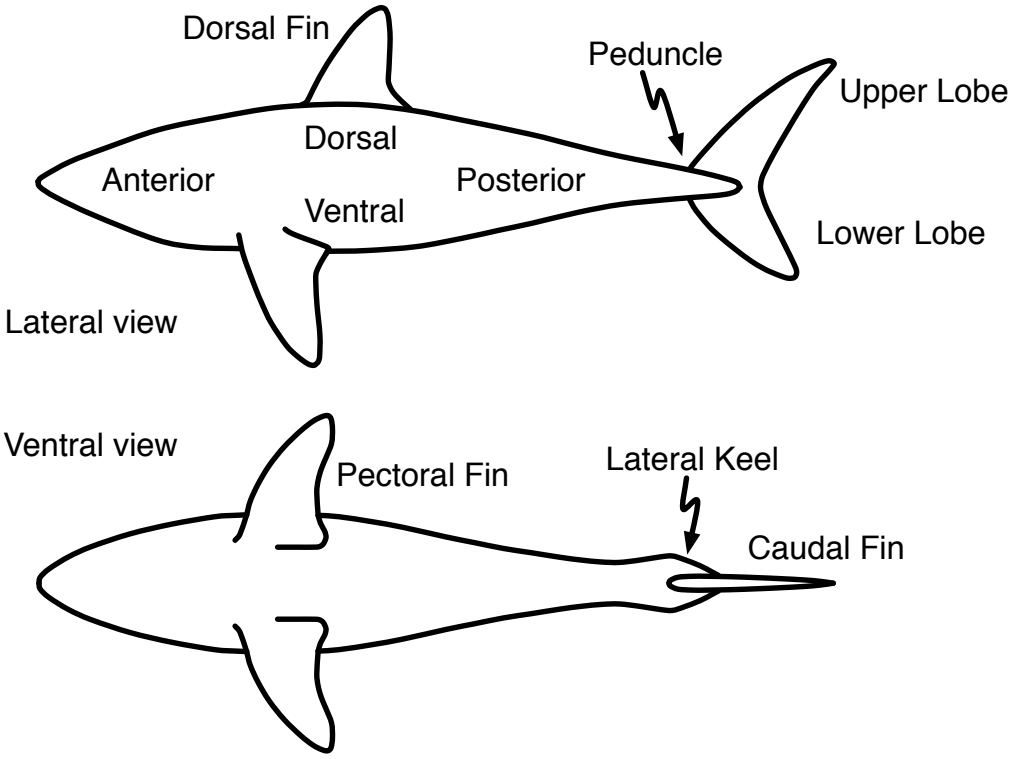

Figure 2-1: Relevant fish anatomy, outline shown is that of a salmon shark (*Lamna ditropis*).

The pectoral fins are generally positioned forward of the body's mass and buoyancy centers, and may be used for propulsion, to counter body weight by producing lift, or for maneuvering. Some species, like tuna for example, have flexible pectoral fins

positioned near the center of their bodies in the dorsoventral direction and are able to fold them against the sides of the body to reduce drag while cruising. On the other hand, sharks have stiff, ventrally-positioned pectoral fins that are angled downward from the body's lateral plane at what is called a dihedral angle, a term that is also used for similarly configured aircraft wings. For many fish, the roles of the pectoral fins are analogous to those of an aircraft's wings (including the ailerons and flaps) and elevators (or canards) all combined.

Dorsal and ventral fins provide roll and yaw stability while swimming. The degree of flexibility in these fins varies greatly among fish species, however they are normally passive features in that they aren't manipulated by muscles while swimming.

For many species, the caudal fin is the primary source of thrust. Fish with symmetric upper and lower caudal lobes, such as tuna, are said to have homocercal tails, while those with asymmetric lobes, such as sharks, are said to have heterocercal tails. For homocercal tails, thrust is directed along the body's centerline in the dorsoventral plane, while heterocercal tails tend to produce a downward pitching moment on the body, as shown in Figure 2-2, which must be balanced by a an opposing moment for level swimming.

The portion of the body just anterior of the caudal fin is called the peduncle, or caudal peduncle. From the lateral view, the peduncle appears narrow, which serves to minimize drag in the direction of tail motion during swimming. When viewed from the dorsal or ventral direction, the peduncle has a much wider profile, which is called the lateral keel. The lateral keel both provides pitch stability, like the tail plane on an aircraft, and transmits power from the body's posterior muscles to the

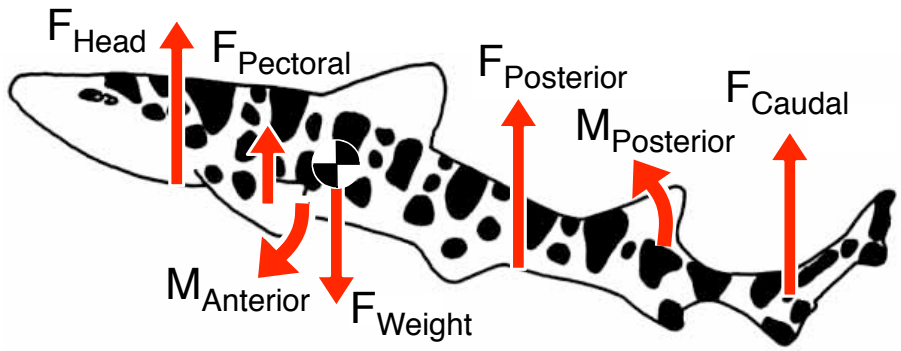

Figure 2-2: Forces and moments acting on a leopard shark (*Triakis semifasciata*). The negative pitching moment from heterocercal tail is countered by a positive moment produced by the pectoral fins and anterior body dorsoventral asymmetry. Adapted from [52].

caudal fin.

2.1.2 Swimming Styles

In terms of propulsive styles, fish may be divided into two general classes: (i) body and/or caudal fin (BCF) propulsors and (ii) median and/or paired fin (MPF) propulsors [39]. BCF propulsive modes may be categorized as anguilliform, subcarangiform, carangiform, or thunniform. A graphic summarizing the classes of BCF swimmers is provided in Figure 2-3.

Anguilliform locomotion involves undulations which travel along the body. These swimmers typically have long, slender bodies with cross-sectional areas that vary little along the longitudinal body axis. Examples of anguilliform swimmers are marine snakes, eels and lampreys.

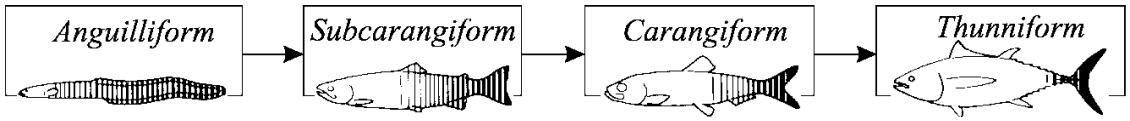

Figure 2-3: Spectrum of BCF propulsors. Adapted from [39].

At the opposite end of the BCF sub-spectrum are carangiform and thunniform swimmers for which body motions are mostly restricted to oscillations of the posterior third of the body. Characteristic of such swimmers are high aspect ratio, lunate tails and spindle-shaped bodies; morphologies adapted for efficient swimming at high-speeds for sustained periods of time. Examples of thunniform swimmers include carp, tuna, and sharks. Although this work focuses on thunniform swimmers, much of the content may be extended to other BCF propulsors.

In contrast to BCF types, MPF propulsion is best suited for positioning and maneuverability at low-speeds. Examples of MPF swimmers range from batoids, skates (rajiform) and pelagic rays (mobuliform), to sunfish and lion fish. MPF swimming is not considered in this work, however due to the model's modular nature, the methods may be readily adapted to devices using this form of propulsion.

2.2 Salient Aspects of Fish Swimming

Scientific minds have long been intrigued by the mechanics of fish-like propulsion. One of the earliest analyses of the mechanics of swimming fish was published by Taylor in the 1950s [43]. However, it was only several years later that Lighthill developed his so-called "slender body theory" [23, 24, 25], an analytical small-amplitude dis-

placement model, which he later extended to form the "elongated-body theory" [26] that is still used today as the basis for various studies of fish swimming [27], [40].

While elegant in its own right, slender body theory is not without limitations. In addition to the small-displacement and slender-body constraints, the model assumes that the swimming is maintained at a constant speed and in the direction parallel to the body's longitudinal axis. Furthermore, thrust and power considerations are taken as the time averages, which is only truly appropriate for periodic motions.

There is a wealth of publications concerning the hydrodynamic mechanisms exploited by fish while swimming [12], [39], [40]. Lighthill's work was some of the earliest to consider the role of shed vortices in fish propulsion, but lacked quantitative measurements of the fluid dynamics due to the technological limitations of the time. Advancements in non-intrusive fluid measurement techniques such as digital particle image velocimetry (DPIV) and particle tracking velocimetry (PTV) [34], have allowed investigators to carry out quantitative analyses of swimming hydrodynamics [15], [21], [22], [30], [52], [53], [54], [55].

Contrary to popular belief, the caudal fin is not solely responsible for the production of thrust. In fact, the formation of the propulsively-linked vortex jets depends heavily on how the body moves. Based on a combination of DPIV and PTV measurements, the undulating lateral motions of a fish's body are seen to create a pumping action, drawing fluid around and along the body [30] as illustrated in Figure 2-4. Once the circulating flow reaches the caudal fin, it interacts with vortices generated by tail movements, resulting in the signature trailing vortices. As the fish swims forward, a propulsive jet zig-zags between the alternating shed vortices, producing a net forward thrust on the body. Models of fish-like body dynamics in both two- [47], [50], [51]

and three-dimensions [9], [10], [11], [58] exist, however they either require limiting assumptions to be made about the fish geometry, composition, and swimming behaviour, or are overly complex, consisting of systems of partial differential equations requiring numerical solutions.

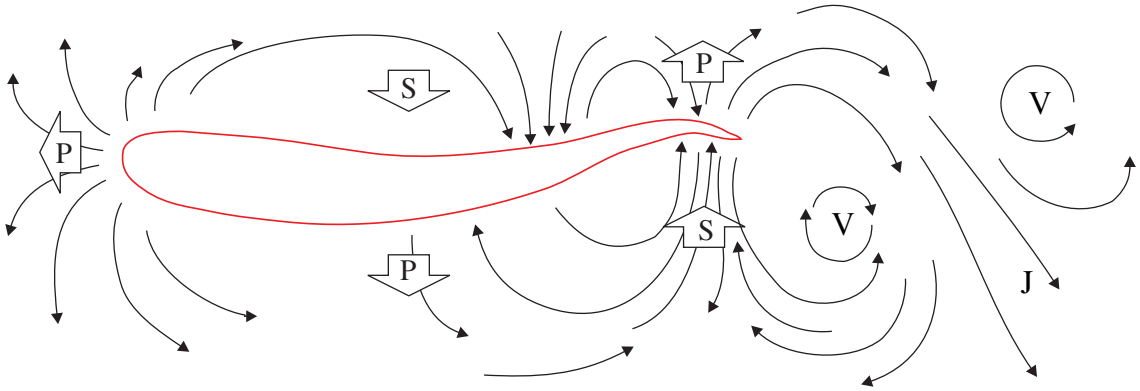

Figure 2-4: Schematic of the flow pattern around a swimming mullet (*Chelon labrosus*). Suction and pressure regions are labeled with "S" and "P", respectively. Arrows indicate flow direction. Shed vortices and the propulsive jet are labeled with "V" and "J", respectively. Adapted from [30].

Kinematics-based analyses, [6], [14], [21], [50] of fish in controlled laboratory environments have given invaluable insight into how different species move under various circumstances. The body kinematics are often augmented with thrust estimates based on mass and acceleration measurements.

2.3 Fish-like Devices

In its most distilled form, the mechanism used by fish to generate thrust may be partially emulated using a flapping foil. Various studies [35], [36], [37], [42], [45],

[56] have explored thrust production by way of shed vortices using engineered hydrofoils undergoing pitching and heaving motions. An example of the flapping foil test apparatus used in [35] is shown in Figure 2-5.

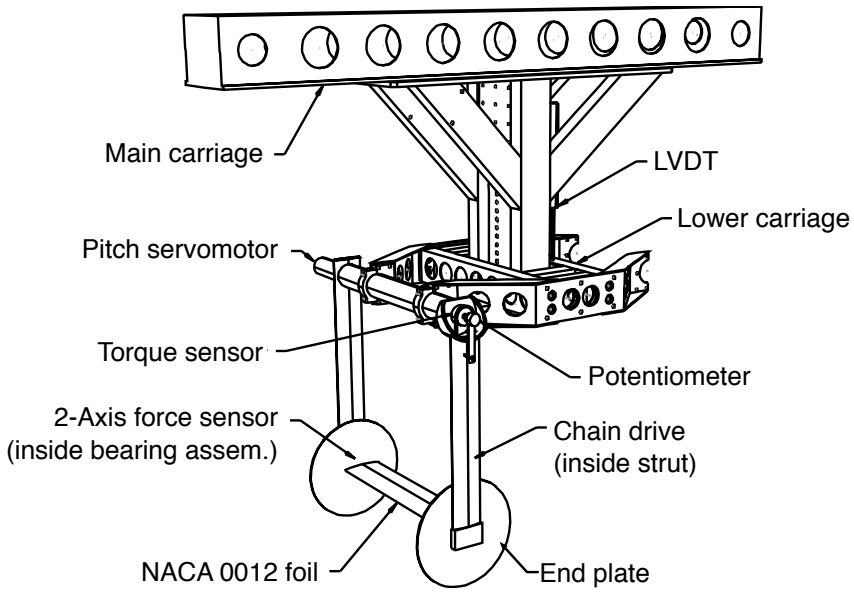

Figure 2-5: Test apparatus typically used for pitching and heaving foil experiments. Tip-mounted end plates minimize 3-dimensional flow effects due to leakage. Adapted from [35].

Drawing upon published results from studies of flapping foils and fish kinematics, a number of biomimetic swimming devices have been successfully constructed. Perhaps the most famous is the Massachusetts Institute of Technology (MIT) Robotuna [4], [5] and its free swimming successor, the Vorticity Control Unmanned Undersea Vehicle (VCUUV) [2], [3], which were both large thunniform swimmers with jointed tails, the latter of which was actuated by powerful internal hydraulics.

In recent years, a shift has been observed towards smaller devices capable of carrying

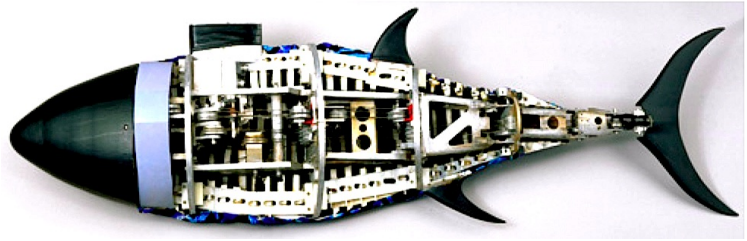

Figure 2-6: A look inside MIT's Robotuna. The device weighed nearly 20 kg and measured nearly 0.9 m in length. The articulated tail was comprised of a series of rigid links actuated by "mechanical tendons", which consisting of a number of pulleys, motors, and cables. Adapted from [38].

embedded sensors and computers, giving rise to a new breed of remotely operated vehicle (ROV), and in some instances, autonomously operated vehicle (AUV) [18], [28], [29].

A unique subclass of swimmer that exploits viscoelastic beam dynamics for propulsion while requiring only a single actuator was recently developed by Valdivia at MIT [47], [48], [49]. The work presented here is primarily focused on swimmers of this type.

Chapter 3

Model Development

The task of modeling the dynamics of a submerged, compliant body is a formidable challenge. Due to the complex hydrodynamic coupling and viscoelastic material properties, a closed-form solution for the resulting system of nonlinear partial differential equations is out of the question. Order-of-magnitude lumped parameter models may be suitable for material selection and initial performance estimates [47], however higher-fidelity models are desirable for control system design and system optimization.

In this chapter, a modeling scheme based on the notion of engineering primitives is presented. Engineering conventions borrowed from both aircraft and nautical vessels are adapted to suit a rather unconventional class of submersible devices.

3.1 Simplifying Constraints

A number of simplifications are made in order to make the problem of modeling swimmers a tractable one. In this discussion, the following key assumptions hold:

1. The water surrounding the swimmer is incompressible $\frac{D\rho_f}{Dt} = 0$.
2. The moving body is incompressible, $\frac{D\rho_b}{Dt} = 0$.
3. The Earth is fixed in inertial space, permitting the use of an inertial reference frame, Σ_i.
4. Gravity is considered to be uniform, resulting in coincident swimmer center of mass and center of gravity.

The above simplifications are standard affair in many aircraft and submersible analyses and are well suited for the biomimetic swimmers considered here.

3.1.1 Engineering Primitives

With the liberties presented in Section 3.1, it is convenient to pursue a modular modeling strategy. Before moving on, it behooves us to explicitly define the notion of engineering primitives in the present context by way of analogy.

In computer graphics, geometric primitives include elementary shapes, such as circles, triangles, and squares. By combining and manipulating these shape primitives, it is possible to construct more complex geometries. For example, one might model

a cylinder by defining two circles as its ends. A more relevant analogy would be that of using mass, spring, and damping primitives to represent complex mechanical systems, like a vibrating beam on a viscoelastic foundation. For the purpose of modeling compliant biomimetic swimmers, the following palette of high-level engineering primitives may serve as a basis:

1. Rigid body hydrodynamics

2. Flapping lifting surfaces

3. Body-fixed lifting surfaces

To assist in organizing the model development, the swimmer is divided into a number of modules, as seen in Figure 3-1. Solid and dashed arrows in the figure represent primary and secondary channels of energy flow between modules, respectively. The secondary energy flows may include trailing vortices or turbulent wakes formed by the pectoral fins and seen by the tail, and flow reversal at the pectoral fins due to heavily biased tail motions. Primitives are used for developing models for each module.

The tail is considered to obey a causal relationship with its actuation source, which resides in the body. For the case where the actuator is a servomotor, it is assumed to be capable of providing as much torque as is needed to move the drive tail to a desired position.

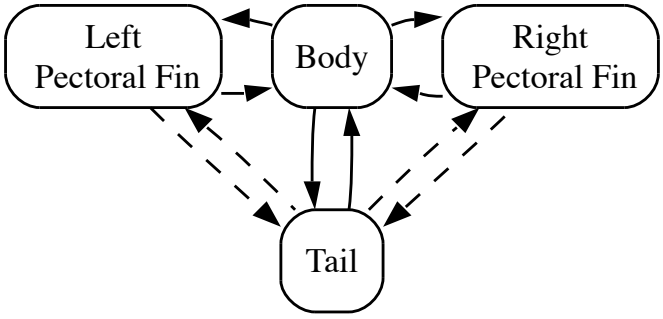

Figure 3-1: Model module interaction, secondary coupling indicated by dashed lines (environmental coupling not shown).

3.2 Rigid Body Motion

To facilitate modeling the motion of a swimmer, we consider a rigid object with the mass and volumetric properties that are reminiscent of those of the swimmer in its undeformed, or "stretched-straight" [23], state.

3.2.1 Coordinate Systems

Three rectilinear coordinate systems, shown in Figure 3-2, are used to describe the motion of the rigid body swimmer model through space, the first of which is the Earth-fixed inertial reference frame $\Sigma_i \in \Re^3$ whose origin is denoted by O_i. The second coordinate system is the body-fixed reference frame $\Sigma_b \in \Re^3$ whose origin O_b is fixed to the rigid body such that it moves with the body throughout the domain spanned by the inertial reference frame. The third coordinate system, $\Sigma_c \in \Re^3$, corresponds to the observer reference frame and has an origin O_c that, like O_b, that

may move within Σ_i.

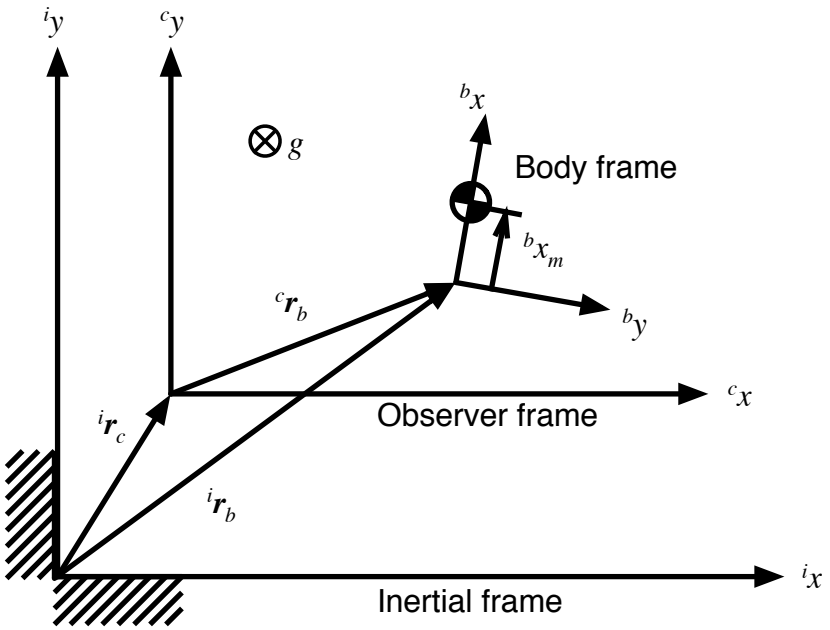

Figure 3-2: Inertial, body, and observer coordinate frames. Gravity is shown pointing into the page.

The position of O_i in space is arbitrary, and we consider the orientation of Σ_i to be such that its $^i z$-axis is aligned with the direction of Earth's gravity. The $^i x$- and $^i y$-axes span the horizontal plane.

The position of O_b is fixed to the rigid body and assigned an orientation such that the $^b x-$axis is aligned with the body's longitudinal axis and points towards the nose of the device, the $^b y$-axis is directed laterally, and the $^b z$-axis is directed ventrally. The body's center of mass is located at a position $^b \boldsymbol{r}_m$ with respect to O_b, and the center of buoyancy at $^b \boldsymbol{r}_B$.

The vector of body position coordinates ${}^{i}\boldsymbol{r}_b \in \Re^3$ is defined with respect to Σ_i and expressed as,

$$ {}^{i}\boldsymbol{r}_b = \begin{bmatrix} x & y & z \end{bmatrix}^{\mathsf{T}}. \tag{3.1} $$

Taking the derivative with respect to time, we obtain the translational velocity components of O_b with respect to Σ_i,

$$ {}^{i}\dot{\boldsymbol{r}}_b = \frac{d}{dt}\begin{bmatrix} x & y & z \end{bmatrix}^{\mathsf{T}} = \begin{bmatrix} \dot{x} & \dot{y} & \dot{z} \end{bmatrix}^{\mathsf{T}}. \tag{3.2} $$

The translatory velocity components of O_b with respect to the inertial frame, but in the directions of the body frame axes, are,

$$ {}^{b}\boldsymbol{v}_b = \begin{bmatrix} u & v & w \end{bmatrix}^{\mathsf{T}}. \tag{3.3} $$

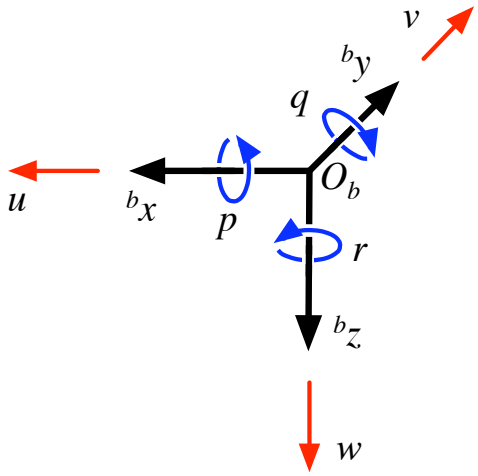

Figure 3-3: Body translational and rotational velocity components relative to the inertial frame and projected onto the body frame axes.

Since the body frame is free to rotate relative to the inertial frame, it is necessary to introduce a rotation matrix ${}^{b}\mathbf{R}_{i}$ linking the inertial and body frame orientations. The translational velocity components may be transformed between the two frames via the following matrix equation,

$$ {}^{b}\boldsymbol{v}_{b} = {}^{i}\mathbf{R}_{b}\,{}^{i}\dot{\boldsymbol{r}}_{b}. \tag{3.4} $$

Euler angles and quaternions are often used to represent body frame orientation relative to the inertial reference frame. Despite their susceptibility to the so-called "gimbal lock" condition caused by singularities, Euler angles will be used since they provide clearer physical insight. We now define the attitude vector ${}^{i}\boldsymbol{\phi}_{b} \in \Re^{3}$ as the vector of the body's Euler angles in the inertial reference frame, where

$$ {}^{i}\boldsymbol{\phi}_{b} = \begin{bmatrix} \phi & \theta & \psi \end{bmatrix}^{\mathsf{T}}. \tag{3.5} $$

The aforementioned rotation matrix ${}^{i}\mathbf{R}_{b}$ may be written in terms of the Euler angles as

$$ {}^{i}\mathbf{R}_{b} = \begin{bmatrix} c_{\psi}c_{\theta} & s_{\psi}c_{\theta} & -s_{\theta} \\ -s_{\psi}c_{\phi} + c_{\psi}s_{\theta}s_{\phi} & c_{\psi}c_{\phi} + s_{\psi}s_{\theta}s_{\phi} & s_{\phi}c_{\theta} \\ s_{\psi}s_{\phi} + c_{\psi}s_{\theta}c_{\phi} & -c_{\psi}s_{\phi} + s_{\psi}s_{\theta}c_{\phi} & c_{\phi}c_{\theta} \end{bmatrix}, \tag{3.6} $$

where $c_{(\cdot)}$ and $s_{(\cdot)}$ denote $\cos(\cdot)$ and $\sin(\cdot)$, respectively. Since ${}^{i}\mathbf{R}_{b}$ is orthonormal, the reverse transformation, from the body-fixed reference frame to the inertial reference frame, may be accomplished by simply taking the transpose, since

$$ {}^{i}\mathbf{R}_{b}^{-1} = {}^{i}\mathbf{R}_{b}^{\mathsf{T}} = {}^{b}\mathbf{R}_{i}. \tag{3.7} $$

The angular velocity components of the body with respect to the inertial reference frame, but aligned with the body axes are

$$ {}^{b}\boldsymbol{\omega}_{b} = \begin{bmatrix} p & q & r \end{bmatrix}^{\mathsf{T}}. \tag{3.8} $$

The time derivative of the attitude vector is the Euler rate vector,

$$ {}^{i}\dot{\boldsymbol{\phi}}_{b} = \begin{bmatrix} \dot{\phi} & \dot{\theta} & \dot{\psi} \end{bmatrix}^{\mathsf{T}}, \tag{3.9} $$

which is related to the body-fixed angular velocity by an appropriate transformation matrix ${}^{b}\mathbf{L} \in \Re^{3\times 3}$, where

$$ {}^{b}\boldsymbol{\omega}_{b} = {}^{b}\mathbf{L}\ {}^{i}\dot{\boldsymbol{\phi}}_{b}. \tag{3.10} $$

When expressed in terms of Euler angles, the transformation matrix is

$$ {}^{b}\mathbf{L} = \begin{bmatrix} 1 & 0 & -s_{\theta} \\ 0 & c_{\phi} & c_{\theta}s_{\phi} \\ 0 & -s_{\phi} & c_{\theta}c_{\phi} \end{bmatrix}. \tag{3.11} $$

To determine the body's angular rates in terms of the inertial frame's axes, one may simply use the rotation matrix given by (3.6).

The observer frame Σ_c may be related to the inertial frame using methods similar to those given for relating the body-fixed reference frame.

3.2.2 Rigid Body Dynamics

The vector of body translational accelerations with respect to the inertial reference frame, but projected onto the body axes is given by

$$\frac{d}{dt}({}^{b}\boldsymbol{v}_b) = {}^{b}\dot{\boldsymbol{v}}_b = \begin{bmatrix} \dot{u} & \dot{v} & \dot{w} \end{bmatrix}^{\mathsf{T}}. \tag{3.12}$$

Similarly, the body's angular acceleration components with respect to the inertial reference frame and projected onto the body axes are

$$\frac{d}{dt}({}^{b}\boldsymbol{\omega}_b) = {}^{b}\dot{\boldsymbol{\omega}}_b = \begin{bmatrix} \dot{p} & \dot{q} & \dot{r} \end{bmatrix}^{\mathsf{T}}. \tag{3.13}$$

Inserting (3.12) and (3.13) into the Newton-Euler equations of motion, we obtain the following

$$\sum_k \boldsymbol{F}_k = m_b \left[{}^{b}\dot{\boldsymbol{v}}_b + {}^{b}\boldsymbol{\omega}_b \times {}^{b}\boldsymbol{v}_b + {}^{b}\dot{\boldsymbol{\omega}}_b \times {}^{b}\boldsymbol{r}_m + {}^{b}\boldsymbol{\omega}_b \times \left({}^{b}\boldsymbol{\omega}_b \times {}^{b}\boldsymbol{r}_m \right) \right] \tag{3.14}$$

$$\begin{aligned} \sum_k \left(\boldsymbol{M}_k + {}^{b}\boldsymbol{r}_k \times \boldsymbol{F_k} \right) = {} & m_b {}^{b}\boldsymbol{r}_m \times \left({}^{b}\dot{\boldsymbol{v}}_b + {}^{b}\boldsymbol{\omega}_b \times {}^{b}\boldsymbol{v}_b \right) + \mathbf{I}_b {}^{b}\dot{\boldsymbol{\omega}}_b \\ & + m_b {}^{b}\boldsymbol{r}_m \times {}^{b}\boldsymbol{\omega}_b \left({}^{b}\boldsymbol{\omega}_b \cdot {}^{b}\boldsymbol{r}_m \right) \end{aligned} \tag{3.15}$$

where the terms on the left-hand side are external forces and moments due to gravitational effects and hydrodynamics, including propulsion, or

$$\text{(Net Load)} = \text{(Hydrostatic)} + \text{(Added Mass)} + \text{(Drag)} + \text{(Lift)} + \text{(Propulsion)}. \tag{3.16}$$

These loads are examined in detail later in the chapter.

The external moments comprising the left-hand side of Equation (3.15) are denoted by

$$\sum_k \left(\boldsymbol{M}_k + {}^b\boldsymbol{r}_k \times \boldsymbol{F_k}\right) = \begin{bmatrix} K & M & N \end{bmatrix}^{\mathsf{T}}. \tag{3.17}$$

Substituting (3.17) into (3.15) and then introducing the material inertia tensor

$$\mathbf{I}_b = \begin{bmatrix} I_{xx} & I_{xy} & I_{xz} \\ I_{yx} & I_{yy} & I_{yz} \\ I_{zx} & I_{zy} & I_{zz} \end{bmatrix}, \tag{3.18}$$

we may express the expanded moment equations as

$$\begin{aligned} K = {} & I_{xx}\dot{p} + I_{xy}\dot{q} + I_{xz}\dot{r} + \left(I_{zz} - I_{yy}\right) rq + I_{yz}\left(q^2 - r^2\right) + I_{xz}pq - I_{xy}pr \\ & + m\left[y_m\left(\dot{w} + pv - qu\right) - z_m\left(\dot{v} + ru - pw\right)\right] \end{aligned} \tag{3.19}$$

$$\begin{aligned} M = {} & I_{yx}\dot{p} + I_{yy}\dot{q} + I_{yz}\dot{r} + \left(I_{xx} - I_{zz}\right) pr + I_{xz}\left(r^2 - p^2\right) + I_{xy}qr - I_{yz}qp \\ & + m\left[z_m\left(\dot{u} + qw - rv\right) - x_m\left(\dot{w} + pv - qu\right)\right] \end{aligned} \tag{3.20}$$

$$\begin{aligned} N = {} & I_{zx}\dot{p} + I_{zy}\dot{q} + I_{zz}\dot{r} + \left(I_{yy} - I_{xx}\right) pq + I_{xy}\left(p^2 - q^2\right) + I_{yz}pr - I_{xz}qr \\ & + m\left[x_m\left(\dot{v} + ru - pw\right) - y_m\left(\dot{u} + qw - rv\right)\right] \end{aligned} \tag{3.21}$$

where For instances where the body is symmetric about the ${}^bx{}^bz$-plane, the I_{xy} and I_{yz} terms are zero.

3.3 The Body as a Viscoelastic Beam

Designing compliant fish-like swimming devices by analytically modeling fish bodies as viscoelastic beams with free end conditions was previously developed for the class of compliant swimmers considered here [47], [48], [49]. An inverse kinematics based approach was adopted to determine suitable viscoelastic material properties given both desired body motions and fish morphology. By providing harmonic excitation at a selected point along the body's longitudinal span, the resulting response was shown to produce thrust, propelling the device forward. Optimally, one might construct such devices using engineered materials with properties that varied continuously throughout the body. With manufacturability in mind, a lumped parameter model was developed to represent the fish body.

A schematic of the dorsal view of a fish-like body is provided in Figure 3-4 to assist with the discussion of modeling BCF swimmers as viscoelastic beams. In essence the body segment between the root of the tail, corresponding to the point of actuation, and the caudal fin serves as a nonlinear transmission. The transmission of power is not ideal in that energy is both stored, by inertial and elastic elements, and dissipated by internal viscous elements. Furthermore, interaction with the surrounding fluid introduces an additional set of dynamics, which are discussed later on.

We begin by considering the inertial elements. The body may be decomposed along its length into a series of differential material elements, or slices, of infinitesimal thickness dx, shown in red. Since each slice has a cross-sectional area $A_{cs}(x)$, the

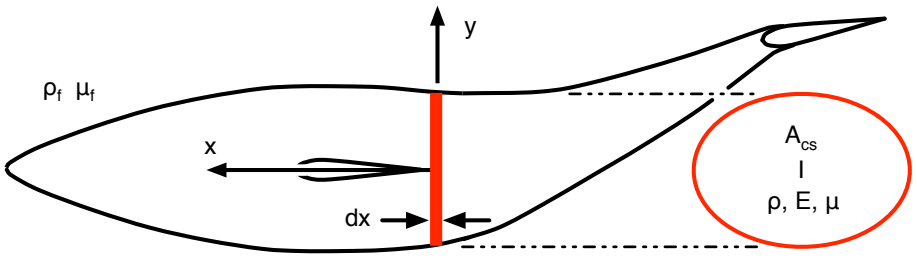

Figure 3-4: Dorsal view of a fish-like body of elliptical cross-section, notation used in the viscoelastic beam model is indicated. The parameters ρ_f and μ_f are the fluid medium's density and dynamic viscosity, respectively.

body's total material mass may be expressed as

$$m_b = \int_0^\ell \rho(x) A_{cs}(x) dx. \tag{3.22}$$

Furthermore, a beam's resistance to bending is related to the area moment of inertia

$$I = \int y^2 dA, \tag{3.23}$$

where the slices are in the xz-direction.

In lumped parameter form, the total material mass may be rewritten as the sum of N component masses,

$$m_b = \sum_{k=1}^{N} m_k = \sum_{k=0}^{N} \rho_k V_k \tag{3.24}$$

where V_k is the finite volume of the k^{th} lumped element.

For a thin beam undergoing sufficiently small transverse deflections, the elemental masses m_k provide a suitable model of a beam's inertial characteristics.

Modeling masses undergoing rotations, requires computation moments and products of inertia. Using indicial notation, we may express the elements of the inertia tensor $\mathbf{I}_b$ for N masses as

$$I_{ab} = \sum_{k=1}^{N} m_k \left[\left(r_{ka}^2 + r_{kb}^2 \right) \delta_{ab} - r_{ka} r_{kb} \right] \tag{3.25}$$

where a and b are dummy indices for the x-, y-, and z-axes, δ_{ab} is the Kronecker delta, and r_{ka} and r_{kb} are the distances along the a- and b-axes from each elemental mass m_k to the point about which the tensor is being computed.

The forced transverse deflections $h(x,t)$ of a vibrating, submerged beam with varying cross-sectional area $A_{cs}(x)$ and uniform material properties (ρ, E, μ) are governed by the following partial-differential equation [47],

$$\rho A_{cs}(x) \frac{\partial^2 h}{\partial t^2} + \frac{\partial^2}{\partial x^2} \left[EI(x) \frac{\partial^2 h}{\partial x^2} + \mu I(x) \frac{\partial}{\partial t} \frac{\partial^2 h}{\partial x^2} \right] = Y_{ext} + F(x,t) \tag{3.26}$$

where $I(x)$ is the area moment of inertia. The three terms on the left-hand side represent the beam's inertia-, compliance-, and damping-related dynamic elements, respectively. On the right-hand side, the term Y_{ext} represents external span-wise loading in the transverse direction, and $F(x,t)$ represents the excitation source. Equation (3.26) cannot readily be solved using analytical methods. Valdivia [47] proposed a solution based on Green's functions, however the method only applies to the case where ρ, E, μ, A_{cs}, and I are constant throughout the length of the body. Like the prototype swimmer developed for this work, the devices modeled by (3.26) used a servomotor as the excitation source. The servomotor was assumed to generate a concentrated time-varying torque at a known position along the length of the body.

While (3.26) serves as an elegant modeling choice for design purposes, it fails to

accurately represent the lateral dynamics of an actual compliant swimmer. When a prototype aircraft is built, it is known that the loads predicted by aerodynamic and structural models used for design will differ from those encountered during actual flight. In order to characterize the true aircraft dynamics, a test pilot runs a gamut of flight maneuvers and experiments while instrumentation measures and logs a myriad of control inputs and sensor outputs. The measured signals are later analyzed to generate the sought after model. A similar concept is explored here, where experimental measurements of the actual swimmer's kinematics are used to develop kinematic models for simulating swimmer motions.

For this work, an approach using Volterra series expansions for identification of kinematics was developed. A causal relationship was assumed between the point of actuation, just posterior of the dorsal fin, and the caudal fin. Using measured kinematics of both the actuation point and the caudal fin, one may generate, to an arbitrary order of accuracy, a finite Volterra series estimating the caudal fin kinematic response given an arbitrary kinematic input at the point of actuation. In fact, for a servo-actuated device the use of kinematics is appropriate since the servoing action is about position rather than torque. Examples of the described kinematic relations are presented in Chapter 5.

Forgoing the beam model, we replace the fish-like body with an ellipsoid representation of equivalent volumetric and inertial properties. To approximate the effects of the actual swimmer's compliance on the body's orientation during swimming, the thrust produced by the tail is resolved into force and torque components, which both vary in magnitude and direction.

We now move on to consider how the swimmer interacts with its fluid environment.

3.4 Hydrostatic Effects

Gravitational effects are felt by the body as external forces and moments due to weight and buoyancy. The gravitational acceleration vector is defined as

$$^{i}\boldsymbol{g} = \begin{bmatrix} 0 & 0 & -g \end{bmatrix}^{\mathsf{T}}. \tag{3.27}$$

The loading due to weight W and buoyancy force B acting on the body are respectively,

$$\boldsymbol{W} = m_b \, {}^{i}\boldsymbol{g}, \tag{3.28}$$

and

$$\boldsymbol{B} = -\rho_f \forall_b \, {}^{i}\boldsymbol{g}. \tag{3.29}$$

It follows that the weight and buoyancy forces, acting at the center of mass ${}^{b}\boldsymbol{r}_m$ and center of buoyancy ${}^{b}\boldsymbol{r}_B$, respectively, are expressed in the body-fixed frame as

$${}^{b}\boldsymbol{F}_W = {}^{b}\mathbf{R}_i \boldsymbol{W}, \tag{3.30}$$

and

$${}^{b}\boldsymbol{F}_B = {}^{b}\mathbf{R}_i \boldsymbol{B}. \tag{3.31}$$

The combined external force and moment vector for both gravitational effects is then

$${}^{b}\boldsymbol{F}_g = -\begin{bmatrix} {}^{b}\boldsymbol{F}_W + {}^{b}\boldsymbol{F}_B \\ {}^{b}\boldsymbol{r}_m \times {}^{b}\boldsymbol{F}_W + {}^{b}\boldsymbol{r}_B \times {}^{b}\boldsymbol{F}_B \end{bmatrix}. \tag{3.32}$$

Fish use a number of devices for buoyancy control. Some species use air bladders

to balance their body weight. To gain additional buoyancy, say after feeding, the fish swim to the surface where they ingest air. This means of buoyancy control has the limitation in that buoyancy may only be reduced when not at the surface. Most species of shark are negatively buoyant and must produce hydrodynamic lift to keep from sinking, however they also have enlarged oil-producing livers which allow them to gradually adjust their buoyancy [8].

For the experimental results presented later on, the dynamics are limited to motions in the horizontal plane. As a consequence, the hydrostatic effects are limited to restoring torques about the ${}^{b}x$- and ${}^{b}y$-axes and bobbing, or heave motions, in the ${}^{b}z$-direction. Motion due to these hydrodynamic loads are negligible due to the swimmer's high center of buoyancy and pectoral fins, which provide a large degree of roll, pitch, and heave damping.

3.5 Hydrodynamic Loads

Models for both acceleration- and velocity-dependent forces and moments are discussed in this section. With the exception of the added mass terms, the hydrodynamic forces and moments are expressed as non-dimensional coefficients using the NASA standard form, where the loads are normalized by the product of the dynamic pressure and reference geometric dimensions.

3.5.1 Added Mass

As a submerged body accelerates, the surrounding fluid is accelerated as well resulting in an apparent increase in the submerged body's mass. This form of hydrodynamic loading is often referred to as added mass. Since we consider the fluid density to be uniform, the added mass is strictly a function of the body's geometry. Strictly speaking there are 36 added mass coefficients, $\widetilde{m}_{ab}$ with $a, b = 1...6$, comprising the full six degree-of-freedom added mass tensor, however due to matrix symmetry only 21 are unique. The hydrodynamic forces F_j and moments M_j acting on a body due to added mass may be concisely expressed using Einstein notation,

$$F_j = -\dot{U}_i \widetilde{m}_{ji} - \epsilon_{jkl} U_i \Omega_k \widetilde{m}_{li} \tag{3.33}$$

$$M_j = -\dot{U}_i \widetilde{m}_{j+3,i} - \epsilon_{jkl} U_i \Omega_k \widetilde{m}_{l+3,i} - \epsilon_{jkl} U_i U_k \widetilde{m}_{li} \tag{3.34}$$

where $i = 1..6$, and $j = 1, 2, 3$. The numerical indices are mapped to the body-fixed axes with $1, 2, 3$ corresponding to translational motions in directions of the ${}^b x$-, ${}^b y$-, and ${}^b z$-axes, and $4, 5, 6$ corresponding to rotational motions about the directions of the ${}^b x$-, ${}^b y$-, and ${}^b z$-axes. There is some redundancy in the above notation in that roll is represented by $U_4 = \Omega_1$, pitch by $U_5 = \Omega_2$, and yaw by $U_6 = \Omega_3$. Surge, sway, and heave velocities are U_1, U_2, and U_3, respectively. The factor ϵ_{jkl} in Equations (3.33) and (3.34) is a Levi-Civita operator representing the following permutations

$$\epsilon_{jkl} = \begin{cases} 1 & \text{if } (i,j,k) = (1,2,3), (3,1,2), (2,3,1), \\ 0 & \text{if } i = j \text{ or } j = k \text{ or } k = i, \\ -1 & \text{if } (i,j,k) = (3,2,1), (1,3,2), (2,3,1). \end{cases} \tag{3.35}$$

Carefully defined body-fixed axes may permit one to exploit a body's geometrical symmetries, causing many of the added mass tensor's terms to vanish. For example, when undeflected, a swimmer with elliptical body cross-sections perpendicular to the body-fixed ${}^b x$-axis exhibits symmetry about the ${}^b x {}^b z$-plane. As a result, $\widetilde{m}_{12} = \widetilde{m}_{14} = \widetilde{m}_{16} = \widetilde{m}_{23} = \widetilde{m}_{34} = \widetilde{m}_{36} = 0$. Furthermore, for the same body and assuming the dorsal and ventral fins share similar geometry and longitudinal position, and that the pectoral fins have zero dihedral angle and lie in the body's lateral plane, the resulting symmetry about the ${}^b x {}^b y$-plane causes $\widetilde{m}_{13} = \widetilde{m}_{24} = \widetilde{m}_{12} = 0$. Since each body cross-section in the ${}^b x$ direction is elliptical we may take $\widetilde{m}_{25}$, $\widetilde{m}_{36}$, $\widetilde{m}_{45}$, and $\widetilde{m}_{56}$ to be approximately zero.

To model the added mass coefficients for lateral motions, we shall invoke a method that is often used in the literature known as the slender-body approximation. For a sufficiently slender body (*i.e.*, body length $\ell \gg$ body width d), the three-dimensional added mass coefficients $\widetilde{m}_{ij}^{3D}$ may be approximated by summing the added mass coefficients of geometrically representative two-dimensional slices $\widetilde{m}_{ij}^{2D}$,

$$\widetilde{m}_{ij}^{3D} = \begin{cases} \int_\ell \widetilde{m}_{ij}^{2D} dx & \text{if } i = j \text{ and } i, j < 5, \\ \int_\ell \widetilde{m}_{ij}^{2D} x^2 dx & \text{if } i = j \text{ and } i, j \geq 5, \\ \int_\ell \widetilde{m}_{ii}^{2D} x^2 dx & \text{if } i = 2, 3 \text{ and } j = 6, \\ \int_\ell -\widetilde{m}_{i-1,i}^{2D} x dx & \text{if } i = 4 \text{ and } j = 5, \\ \int_\ell \widetilde{m}_{i,j-4}^{2D} x dx & \text{if } i = 3 \text{ and } j = 6, \\ \int_\ell \widetilde{m}_{i,j-2}^{2D} x dx & \text{if } i = 4 \text{ and } j = 6, \\ \int_\ell -\widetilde{m}_{i-2,j-4}^{2D} x^2 dx & \text{if } i = 5 \text{ and } j = 6. \end{cases} \tag{3.36}$$

As implied earlier, the $\widetilde{m}_{ji}^{3D}$ coefficients are obtained through matrix symmetry.

For a swimmer of elliptical cross-section with major and minor radii that vary in ${}^{b}x$, the two-dimensional added mass per unit slice is

$$\widetilde{m}_{ij}^{2D}(x) = \pi \rho_f R_i(x) R_j(x). \tag{3.37}$$

For $i = 2$ and $j = 3$, $R_{i=2}(x)$ and $R_{j=3}(x)$ are the major and minor ellipse radii which correspond to the body's ${}^{b}y$- and ${}^{b}z$-axes, respectively.

A limitation of this method is that it does not provide a means of computing the added mass for motions in the direction of maximum length, in this case the body's ${}^{b}x$-axis. Newman [31] provides a graphical means of estimating the longitudinal added mass of an ellipsoidal body.

Although the swimmer's geometry is constantly changing, we assume the added mass remains constant. Once the coefficients are computed, the added mass matrix is combined with the body's material mass and inertia tensor to produce an apparent mass matrix.

3.5.2 Body Lift

A swimming body with dorsoventral asymmetry is prone to producing some amount of hydrodynamic lift even when swimming with its body's longitudinal axis parallel to the relative flow. In nature, such asymmetry is evident in various species of shark [14], [15], [52, 53], like the salmon shark depicted in Figure 2-1. Swimmers with

dorsoventrally symmetric bodies are also capable of producing lift when the flow is not parallel to body's longitudinal axis. The subsequent discussion assumes the swimmers have dorsoventral symmetry.

Furthermore, the scope of this work's experimental analysis is constrained to planar motion situations, making the production of lift by the body negligible in the dorsoventral direction. For swimming in three dimensions, when the body does produce lift in the heave direction, one may resort to using modern vortex-lattice techniques to estimate the lift produced by bodies of arbitrary shape [1].

The production of lift in the body's lateral direction should be considered. The recoil action of a thrust producing fish-like tail will cause the anterior portion of the body to yaw relative to the center of mass' direction of travel. The periodic yaw motion induces a flow component in the body's lateral direction. For aircraft, the direction of this lateral flow component is called as the side slip angle β and may be thought of as the lateral angle of attack.

3.5.3 Drag

For a fully submerged body, the hydrodynamic drag forces may be classified as either parasitic drag or induced drag. The parasitic drag is composed of the skin friction drag and the form drag. The induced drag is due to the production of trailing vortices that result from finite lifting surface dimensions and pressure differentials that accompany the hydrodynamic lift. The net drag on a body is simply the sum

of the individual drag sources, that is to say

$$\begin{array}{ccccccc} \text{Net Drag} & = & \text{Form} & + & \text{Skin Friction} & + & \text{Induced} \\ C_D & = & C_{D_p} & + & C_{D_f} & + & C_{D_i} \end{array} \tag{3.38}$$

Since the swimmers operate in a sufficiently high range of Reynolds numbers, the friction drag component may be omitted since it is much smaller than both either the form or induced drag components.

Near the water surface, moving bodies encounter an additional source of resistance known as wave drag. Momentum is transferred from the moving body to vertically displacing water near the surface. In the presence of a gravitational field, like on Earth, the net effect is that work done by the body's source of propulsion is partially diverted from moving the body forward to lifting the weight of a surrounding volume of water, thus forcing the body exert more effort to achieve a given velocity than if it were fully submerged. Drag due to wave formation is not included here for simplicity, however it may be introduced via (3.38).

The body and pectoral fins, for high angles of attack, are considered to be the main contributors to the overall pressure drag, or

$$C_{D_{pressure}} = C_{D_{p,body}} + C_{D_{p,PF1}} + C_{D_{p,PF2}}. \tag{3.39}$$

For motion in the body-fixed ${}^b x$-${}^b y$ plane, the total drag may be decomposed into a transverse component, which resists motion in the body-reference frame's lateral direction, and an axial component, which resists longitudinal motion.

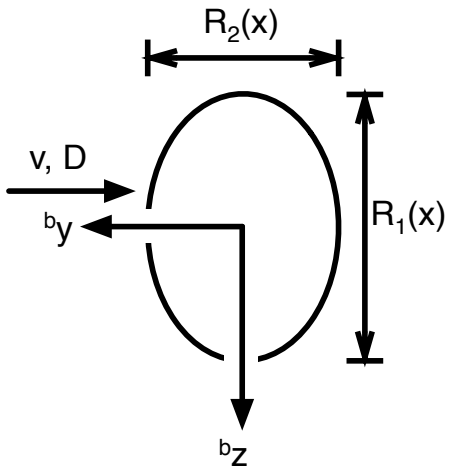

Figure 3-5: Elliptical section drag.

Based on empirical results, the following model has been adapted from [17] for estimating the lower bound for pressure drag of elliptical sections at subcritical Reynolds numbers,

$$C_D \approx 1.1 \frac{R_2(x)}{R_3(x)} \tag{3.40}$$

The model in (3.40) may also be adapted for estimating drag in the longitudinal direction by considering the swimmer's body to be elliptical in the ${}^b x {}^b z$-plane and replacing $R_3(x)$ and $R_2(x)$ with $\ell/2$ and $R_3(x)$, respectively.

3.6 Caudal Fin Model

To motivate the discussion of the caudal fin thrust, we first discuss its geometry.

3.6.1 Caudal Fin Geometry

For simplicity, the caudal fin is considered to be an isolated lifting surface. The prototype swimmer's caudal fin mixes features from different groups of pelagic BCF propulsors, such as the most species of tune, and Carcharhiniform and Lamniform species of shark. Characteristically, these thunniform swimmers have swept-back caudal fins with high aspect-ratios, and narrow caudal peduncles with lateral keels [8]. Caudal fins of pelagic swimmers are often homocercal, and crescent-shaped, like those of tuna shown in Figure 3-6. For sharks, however, the two lobes are quite different – the spine extends into the upper lobe, while the lower lobe is comprised of a flexible and highly elastic collagen matrix. Intuition and the so-called classical model for the production of thrust [14] both suggest that this structural asymmetry produces a torque about the body center of mass causing the nose to pitch downward. This negative pitching moment may be more significant in sharks with less symmetric, heterocercal tails [54], in which the upper lobe is much larger than the lower one. The existence of this torque is related to the hydrodynamics surrounding the *anterior* body, where pectoral fins, and in some species the head, are capable of producing positive pitching moments that must be balanced for forward swimming.

When estimating the lift generated by a lifting-surface of finite span b, one must consider some of the wing's geometric characteristics. The planform area of a full wing span is defined by

$$S = 2\int_0^{b/2} c(y)dy \tag{3.41}$$

where $c(y)$ is the local chord length, which may be a function of the span-wise

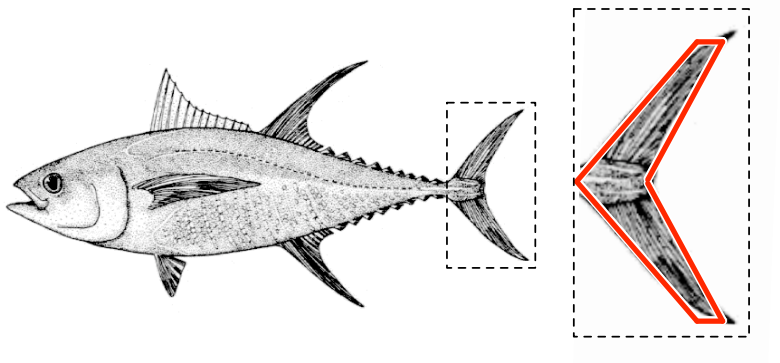

Figure 3-6: Comparing a yellowfin Tuna (*Thunnus albacares*) caudal fin with the planform outline of a swept wing. Adapted from [16].

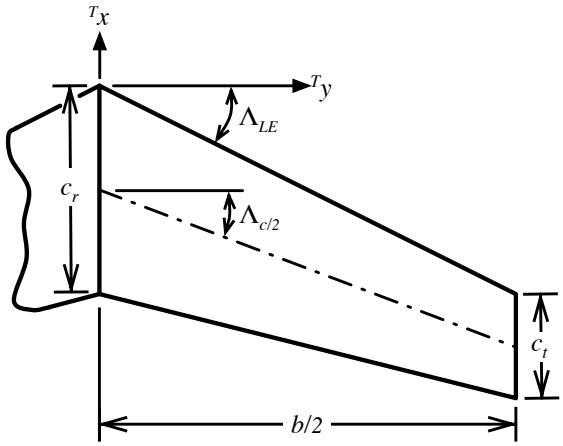

Figure 3-7: Planform view of a lifting surface semi-span. Key dimensions are labeled.

position.

The aspect ratio of a finite lifting surface is defined as

$$\text{Æ}R = \frac{b^2}{S} = \frac{\text{span}^2}{\text{projected area}} \tag{3.42}$$

A morphological characteristic of thunniform swimmers is a high-aspect ratio lunate tail. Both the high speed and efficiency of thunniform propulsors are largely attributed to their caudal planform geometry. To approximate a lunate tail for modeling purposes, we shall consider a swept wing engineering primitive.

In addition to a high aspect ratio, thunniform caudal fins have a small taper ratio defined by

$$\lambda = \frac{c_t}{c_r} = \frac{\text{tip chord}}{\text{root chord}} \tag{3.43}$$

In fact, the tips of thunniform caudal fins are pointed, resulting in a taper ratio of $\lambda_T = 0$. Without loss of generality, the taper ratios for which the lift model is valid are assumed to lie between zero and unity.

3.6.2 Flapping Foil Kinematics

Much of the work regarding flapping foil propulsion has focused on carangiform type swimmers, where oscillatory motions are confined to the last third of the body [39]. Often, said oscillatory motions are modeled as a combination of both periodic pitching and heaving in the caudal fin reference frame [35], [36], whose origin is located at the fin's mean hydrodynamic center. Figure 3-8 depicts a foil undergoing

these two motion. Models of carangiform flapping foil propulsion are applicable to thunniform swimmers due to the many similarities between their swimming styles.

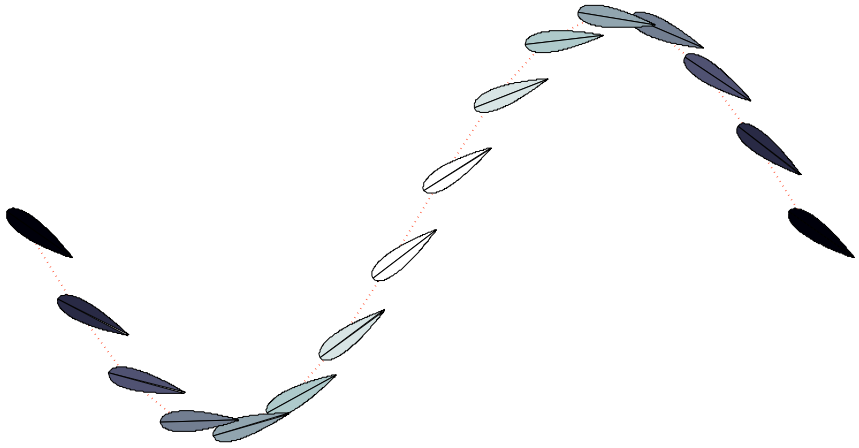

Figure 3-8: Foil undergoing periodic heaving and pitching motions.

The heave motion is described as

$$h_T(t) = H_{To}(t) \sin \omega_T t + h_{Tb}, \tag{3.44}$$

where $H_{To}(t)$ is the heave amplitude, ω_T is the tail beat frequency, t is time, and h_{Tb} is a bias term. For steady maneuvering, such as forward swimming and constant radius turning, H_{To} is time-invariant. Physically, the heave motion is caudal fin's lateral displacement with respect to ${}^b x$.

Similarly, the pitch angle is given by

$$\theta_T(t) = \Theta_{To}(t) \sin(\omega_T t + \phi_T) + \theta_{Tb}, \tag{3.45}$$

where $\theta_{To}(t)$ is the pitch amplitude, ϕ_T is the phase shift between the heave and pitch motions, and θ_{Tb} is a bias angle. The phase shift is generally taken to be around 90° so that the pitch angle leads the heave motion [35]. Physically, the pitch angle corresponds to the angle between the caudal fin's path through space and the direction of body motion.

The caudal fin angle of attack is the angle between the caudal fin's chord line and the apparent flow direction seen by the fin, so it is a function of both the rate of heave $\dot{h}_T(t)$ and the pitch angle

$$\alpha_T(t) = -\tan^{-1}\left[\frac{\dot{h}_T(t)}{{}^b u_T(t)}\right] + \theta_T(t) \tag{3.46}$$

where ${}^b u_T(t)$ is the tail-relative velocity component of the swimming velocity projected on the body-fixed frame. Figure 3-9 shows how the heave rate may induce an angle of attack although the flow is parallel to the foil's chord line.

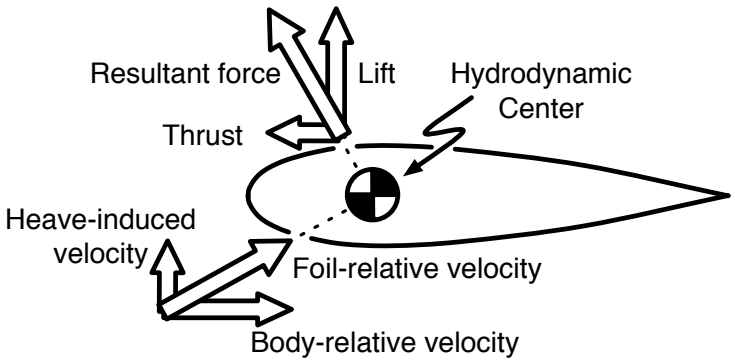

Figure 3-9: Velocity and force components relative to foil-fixed frame.

3.6.3 Lifting Surface Dynamics

The unsteady dynamics of the caudal fin motions may be described non-dimensionally by the Strouhal and Reynolds numbers. The Strouhal number compares the magnitude of the unsteady lateral motions to the forward motion and is defined as

$$St_T = \frac{\langle H_{To} \rangle \omega_T}{\langle {}^b u_T \rangle}, \tag{3.47}$$

where $\langle {}^b u \rangle$ is the average forward velocity in the body-fixed reference frame. The Reynolds number represents the ratio of inertial forces to viscous forces and is defined as

$$Re_{\bar{c}_T} = \frac{\langle {}^b u_T \rangle \bar{c}_T}{\nu_f}, \tag{3.48}$$

where $\bar{c}_T$ is the chord length at the mean hydrodynamic center, and ν_f is the kinematic viscosity of water.

The caudal fin cross-section may be approximated as a symmetric NACA profile $y(x_n)$ defined by

$${}^T y(x_n) = \frac{tc}{2}\left(0.2969 x_n^{1/2} - 0.126 x_n - 0.3516 x_n^2 + 0.2843 x_n^3 - 0.1015 x_n^4\right), \tag{3.49}$$

where

$$x_n(x) = \frac{{}^T x}{c} \tag{3.50}$$

is the non-dimensional chord length, ${}^T x$ is the chord-wise coordinate relative to the caudal fin-fixed reference frame (see Figure 3-7), and t is the maximum foil thickness. The last two digits of a four-digit NACA foil correspond to the maximum thickness as a percentage of the local chord length c. The first two digits correspond to the

foil camber, however only symmetric foils are considered here, so these leading digits are both taken to be zero.

For moderate angles of attack α, the lift of a wing increases with angle of attack in a fairly linear manner. For wings of finite aspect ratio and nontrivial sweep angle, Kuchemann proposed the following equation for estimating the lift curve slope [1],

$$a = \frac{\partial C_L}{\partial \alpha} = \frac{a_o \cos \Lambda_{1/2}}{\sqrt{1 + \left[\frac{a_o \cos\left(\Lambda_{1/2}\right)}{\pi \mathcal{AR}}\right]^2 + \left[\frac{a_o \cos\left(\Lambda_{1/2}\right)}{\pi \mathcal{AR}}\right]}} \tag{3.51}$$

where a_0 is the lift-curve slope for the lifting surface's cross-sectional foil, and $\Lambda_{1/2}$ is the mid-chord sweep angle. Equation (3.51) is really a modified version of the Helmbold equation, which is based on classical lifting-line methods.

The lift coefficient, C_L is dependent on the type of NACA foil being used. The instantaneous caudal fin lift may be estimated as

$$C_{L_T} = a_T \alpha_T \tag{3.52}$$

where the product of the caudal fin relative dynamic pressure based and the planform area may be used to convert the coefficient to its dimensional form.

Borrowing from aeronautical analysis, the instantaneous caudal fin induced drag is roughly modeled as

$$C_{D_{i,T}} = \frac{C_{L_T}^2}{\pi \mathcal{AR}_T \eta_T} \tag{3.53}$$

where η_T is the known as the Oswald Efficiency factor and is based on the assumed lift distribution.

3.7 Pectoral Fin Model

Although fish have flexible pectoral fins with numerous degrees of freedom, we shall constrain our analysis to rigid fins that are only capable of rotating about their spanwise axis. In doing so, we may use a similar lifting surface engineering primitive that was developed for the caudal fin with the exception that the pectoral fins do not undergo heave motion relative to the body reference frame. Many pelagic sharks have plesodic pectoral fins, which are stiff due to internal skeletal support - an example of which may be seen in Figure 3-10. These fins are well suited for fast-swimming pelagic fish since a they provide an efficient source of lift during periods of sustained cruising. On the other hand, aplesodic fins are specialized for accelerating and maneuvering [55].

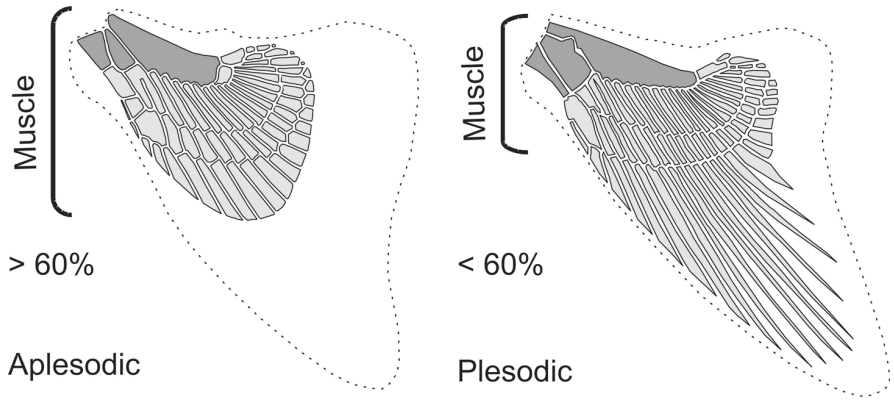

Figure 3-10: A comparison between aplesodic and plesodic pectoral fin skeletal structures. From [55].

Like the caudal fin, the pectoral fins are modeled as isolated lifting surfaces fixed to the body each with mean-aerodynamic centers at a position ${}^{b}\boldsymbol{r}_{PFk}$, $k = 1, 2$, with respect to the body frame. Following the success of others in the literature [28, 29]

a quasi-steady approach is taken for estimating lift and drag forces. The side slip angles β_{PFk} seen by the fins are taken as zero.

The pectoral fin drag coefficients $C_{D_{PFk}}$ are modeled as composites of both pressure and induced drag. The pressure drag is coarsely modeled as a that of a flat plate whose area is equal to the projected area of the fin in the direction of the flow. The induced drag is computed using equation (3.53).

Since there is no dihedral or anhedral angle, the pectoral fins are assumed to produce zero loading in the body's lateral direction.

3.8 The Equations Assembled

Once the hydrodynamic lift and drag have been modeled for each primitive, they must be projected from the flow-relative axes onto the body axes. For example, for the pectoral fins, we may write The longitudinally directed hydrodynamic loading for each fin is given by

$$C_{X_{PFk}} = C_{L_{PFk}} \sin \alpha_{PFk} - C_{D_{PFk}} \cos \alpha_{PFk} \tag{3.54}$$

where $C_{L_{PFk}}$ and $C_{D_{PFk}}$ are the lift and drag forces normalized by $\frac{\rho_w}{2} \|^b \boldsymbol{v}_b\|^2 S_{PF}$, with S_{PF} being the planform area of the full pectoral fin span, and α_{PFk} are the flow-relative angles of attack seen by the pectoral fins. Similarly, the dorsoventrally directed loading may be expressed as

$$C_{Z_{PFk}} = -C_{L_{PFk}} \cos \alpha_{PFk} - C_{D_{PFk}} \sin \alpha_{PFk} \tag{3.55}$$

Once all of the hydrodynamic forces have been projected onto the body axes, the corresponding moments about O_b may be computed. For example, the lift from the pectoral fins acts at each half-span's mean hydrodynamic center. For the general case, this results in both pitch and roll moments about the body's origin.

The assembled hydrodynamic loads may be expressed concisely in the following form

$$X = q_B S_{PF} \left(C_{X_B} + C_{X_{PF1}} + C_{X_{PF2}} \right) + q_T S_T C_{X_T} \tag{3.56}$$

$$Y = q_B S_{PF} C_{Y_B} + q_T S_T C_{Y_T} \tag{3.57}$$

$$Z = q_B S_{PF} \left(C_{Z_B} + C_{Z_{PF1}} + C_{Z_{PF2}} \right) \tag{3.58}$$

$$K = q_B S_{PF} b_{PF} \left(C_{K_B} + C_{K_{PF1}} + C_{K_{PF2}} \right) \tag{3.59}$$

$$M = q_B S_{PF} \bar{c}_{PF} \left(C_{M_B} + C_{M_{PF1}} + C_{M_{PF2}} \right) \tag{3.60}$$

$$N = q_B S_{PF} b_{PF} \left(C_{N_B} + C_{N_{PF1}} + C_{N_{PF2}} \right) + q_T S_T b_T C_{N_T} \tag{3.61}$$

Prior to combining (3.56) through (3.61) with equations (3.14), (3.15), (3.32), (3.33) and (3.34), Taylor series expansions may be used to approximate the dependence of each of the body referenced hydrodynamic force and moment coefficients on flow speeds (u, v, w, p, q, r) and angles (α, β). The choice of which terms to retain largely depends of the swimmer's geometry and should be considered on a case-by-case basis, however often one only needs to consider the first-order terms.

Chapter 4

Experimental Apparatus

The prototype swimmer was designed to accommodate onboard sensing hardware to enable measurement and logging of input-output data.

A number of constraints limit the degree to which a swimmer may be instrumented. One of the design goals was to achieve near-neutral buoyancy, whilst maintaining sufficient compliance along the length of the device. Most electronics and sensors are negatively buoyant; adding such items to the swimmer reduces the buoyancy margin and may violate the aforementioned design constraint. To offset the weight of sensors, one may wish to include air ballasts in their swimmer design. This is an appropriate solution, so long as the effects of adding such ballasts on the body compliance are considered and accounted for in the design stage. Further details regarding the use of air ballasts may be found in Section 4.4.

Apart from buoyancy concerns, space inside of the swimmer is at a premium, espe-

cially for devices of the size scale considered here. The tail and pectoral fin actuators consume a large portion of the mid-body volume, where the cross-sectional area is largest. For servomotors, actuator size does not scale linearly with body dimensions, so for a given body geometry, larger swimmers may accommodate more sensors since the ratio of the actuator volume to useable internal body volume is lower than for smaller swimmers.

Related to the previous consideration, another constraint on the instrumentation is interference. Multi-axis magnetometers found in digital compasses may be used to measure a swimmer's attitude, however proximity to actuators such as servomotors, which contain permanent magnets, has been found to render magnetometers useless. Sensors, such as MEMS accelerometers and gyros, often used to measure linear accelerations and rotational rates, respectively, may also be affected by interference generated by the motor windings and power electronics.

Ultimately, the decision was made to forgo the use of a conventional inertial measurement unit to measure accelerations and angular rates. Data provided by such sensors would be redundant in light of the capabilities of the measurement system described in the following section.

4.1 Vision System

To capture the body kinematics a vision-based motion-capture system was developed. The system's data acquisition flow is shown in Figure 4-1.

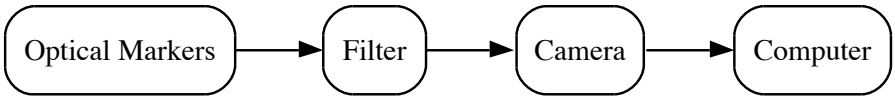

Figure 4-1: Motion capture data acquisition flow.

Typically, commercial motion capture systems use camera-mounted arrays of infrared (IR), or near-IR, light-emitting diodes (LEDs) to flood a stage with IR light. Objects to be tracked are fitted with one or more spherical retro-reflectors. As their name suggests, the basic operating principle behind retro-reflectors is that they reflect incident light rays back to their point of origin. Since the IR LEDs are mounted on the motion capture cameras, the light reflected by the markers is seen by the cameras. Cameras may be fitted with long-pass filters with cut-offs just outside of the near-IR range that includes the LED emission band, thus blocking all but the reflected IR light from reaching the camera's optical sensor. The human eye is not sensitive to light with IR or near-IR wavelengths, however CCD sensors used in motion capture cameras are. Processing of recorded motion-capture video sequences allows one to extract marker trajectories in two-, two-and-one-half-, or three-dimensions, depending on the number of markers and cameras used.

The previously described motion capture methodology may be applied as a means of resolving the compliant swimmers' body kinematics, however a several distinct changes are made. The use of retro-reflective markers is well suited for situations where the camera, LED array, and markers all exist in a common optical medium, such as air. When the camera and LEDs reside in a different optical medium than the markers, problems arise at the interface between the two media should they have different indices of refraction, such as the case of water and air. More specifically,

a fraction of the LED light would be reflected at the water's surface, resulting in false marker detection. The use of polarizing filters may alleviate some but not all of the optical ambiguities resulting from reflected and scattered light. Another option is to use waterproof camera and LED housings, thus eliminating the free surface effects at water-air interface, however limitations due to cost and tank size may be prohibitive. Figure 4-2 illustrates how perturbations at the water surface can lead to optical ambiguities and false positives.

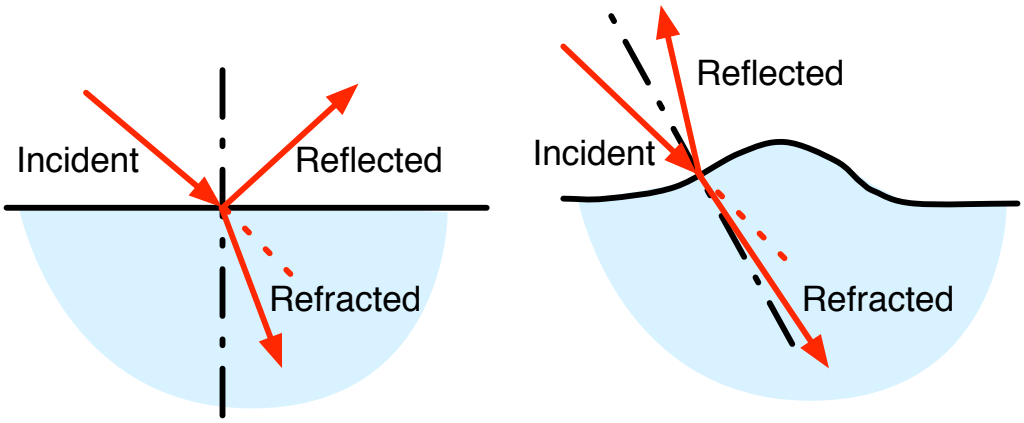

Figure 4-2: Illustration of how surface ripples and waves cause reflections responsible for optical ambiguities. The blue regions represent water, the dash-dot lines indicate the surface normal, and the red vectors represent incident, reflected, and refracted light rays.

A low-cost, alternative approach was developed for tracking swimmers by using active markers rather than passive retro-reflectors to overcome the issue of interfacial reflection. The so-called active markers were simple off-the-shelf wide-angle surface mount IR LEDs, thus the markers emit their own light and alleviate the need for a camera-mounted LED array. The use of wide-angle LEDs reduces the likelihood of the camera loosing sight of individual markers as the swimmer moves around in-

frame. Since the camera is positioned above the tank looking down into the water, the markers are placed along the swimmer's dorsal centerline. In the longitudinal direction, the swimmers are comprised of both flexible and rigid segments, the latter of which contain the onboard electronics, actuators, air ballast, and the caudal fin core. Markers were placed at the interfaces between flexible and rigid segments. An additional marker was placed at the mid-span of flexible segments to improve the accuracy of body deformation curve fits during post-processing. The manner in which the active markers were distributed along the body length is illustrated in Figure 4-3, where the IR LEDs are represented by red circles. Marker lateral displacement h_k and angular deflection θ_k, where $k = 1, 2, ..., 8$, were measured with respect to the ${}^b x$-axis. After experimenting with various candidates, Vishay®VSMG2700 IR LEDs were selected to serve as markers. Specifications of the VSMG2700 LEDs that are relevant to their role as markers are their peak wavelength of 830 nm, compact SMD packaging, and wide $\pm 60^\circ$ angle of half intensity. A pulsed input was used to prevent the LEDs from overheating.

The most obvious drawback of using active markers is the potential risk of water shorting the LED pads or leads, however properly insulated electrical connections all but eliminates this mode of failure. Furthermore, one may implement a means of individually switching markers on or off, say via a shift register or microcontroller GPIO pins, in the event that a localized leak does occur.

In lieu of a specialized motion capture camera, consumer grade USB and IEEE-1394 (Firewire) cameras may be used, largely depending on the required frame rates and spatial resolution. Most cameras of this type include a short-pass filter to block near-IR wavelengths in order to improve colour balance, however such filters must

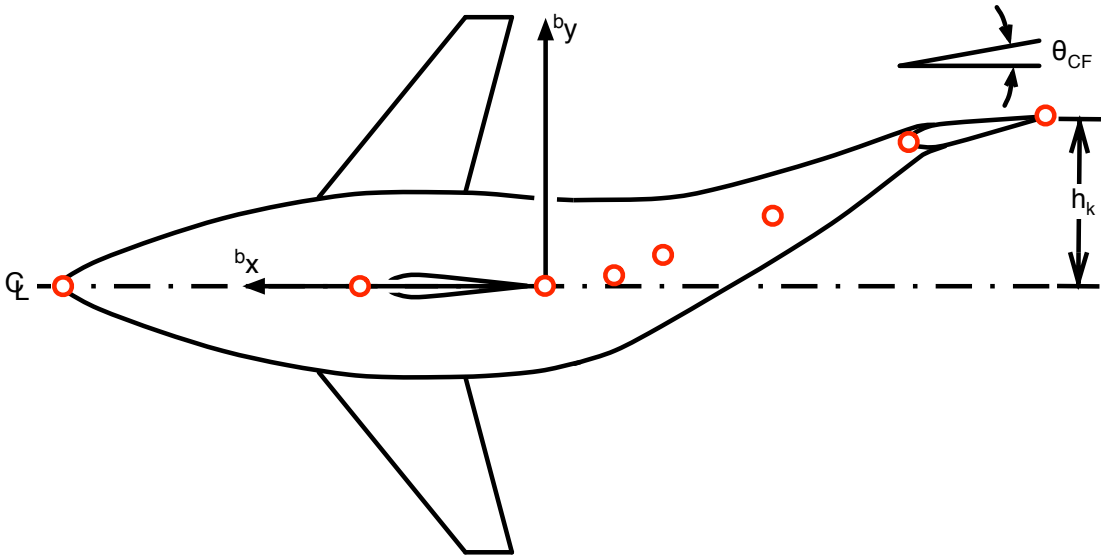

Figure 4-3: Active marker placement relative to body-fixed frame.

be removed if IR light is to be used, as with motion capture methods. Furthermore, grayscale, or so-called black-and-white, cameras are better suited for IR tracking as opposed to models with colour CCDs since only the intensity of the light is of interest. Bayer masks used in most colour CCD cameras reduce the overall intensity of light "seen" by the sensor, thus reducing the camera's overall sensitivity, which may be of concern when the signal-to-noise ratio is low.

USB-based cameras are ubiquitous, however high and steady frame rates are difficult to achieve due to the nature of the Universal Serial Bus specification, which is scheduling based and designed for intermittent bulk data transfers rather than high-capacity data streams, as with the IEEE-1394 specification.

To record the swimmers, two off-the-shelf cameras were considered. The first of which was a Logitech®Quickcam™FUSION 4000, a colour USB camera, which performed

suitably for initial tests and development of the active marker system. However, due to its inability to reliably provide steady frame rate while recording video, this camera was replaced by the IEEE-1394 based Unibrain®Fire-i™Digital Board Camera. The black-and-white variant of the Fire-i™Digital Board Camera, selected for reasons described earlier, features a Sony®ICX-098BL CCD that is capable of providing 640 by 480 pixel images at 30 frames-per-second.

In terms of software, the recordings were made using Apple®iMovie™. The resulting contiguous MPEG-4 video files were then split into individual frames and stored as lossless TIFF files. Processing of the frames was carried out using MATLAB®, the details of which are provided in Chapter 5.

4.1.1 Optics

As mentioned earlier, long-pass filters are often employed in motion capture applications using IR light. The use of such filters drastically increases the signal to noise ratio by allowing light with wavelengths in the near-IR range and longer through whilst blocking shorter wavelengths within the camera CCD's spectral sensitivity range. A custom long-pass filter was fabricated from the storage media of a 3.5-inch floppy diskette. The flexible media consists of a translucent Mylar®substrate, roughly 80 μm thick, with a ferromagnetic iron-oxide coating, roughly 0.9 μm thick. The iron-oxide coating provides the filtering characteristics while the media's meager thickness minimizes any optical distortion. The notion to use floppy disk media for optical filtering was based on prior observations of the dark red tint produced when the media was placed over a bright white light source.

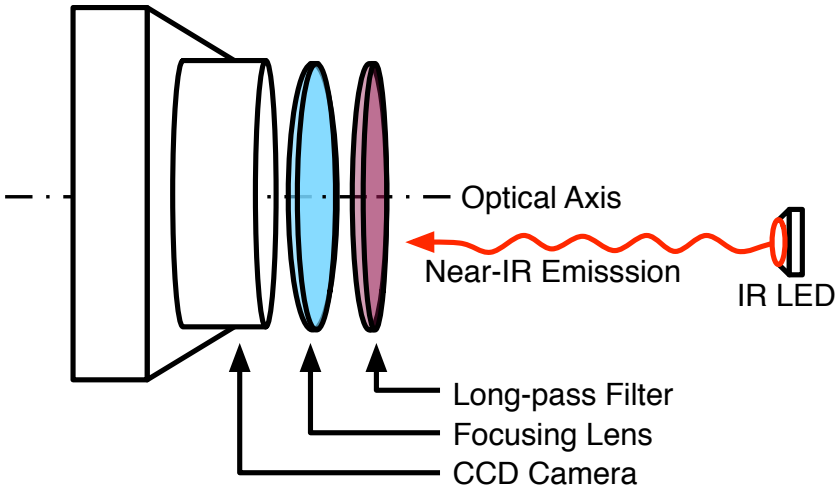

Figure 4-4: Schematic of the vision system's optical flow.

Between the camera CCD and the long-pass filter sits a screw-adjustable focusing lens, as indicated in Figure 4-4. The small 5 mm focal length lens introduces radial and tangential distortion elements into the optical path. A thorough calibration procedure was conducted *in situ* appropriately characterized and model both lens distortion and optical axis misalignment so that recorded image sequences could be corrected prior to extracting marker positions.

4.1.2 Camera Dolly

The narrow field of view provided by the camera was sufficient for constrained kinematic analysis, in which the swimmer's head is held in place by a fixture permitting the posterior half to move freely, but preventing the body-fixed frame from translating relative to inertial frame. To permit motion capture in unconstrained, or free

swimming, conditions, a camera dolly system was devised. Figure 4-5 indicates the main features comprising the dolly. A rigid 80/20®aluminum beam served as the dolly rail and spanned the full 2.6 m length of the swimmer test tank. Long glass strips were secured to the top faces of the rail to provide a smooth surface for the four New Way®air bearings from which the camera was suspended. The dolly system permitted the camera to follow the swimmer along the length of the tank, while The camera's field of view was wide enough to fully cover the 0.6 m width of the tank. As a result, the camera only needed to pan along the tank's length, corresponds to the inertial frame's ${}^{i}y$ axis.

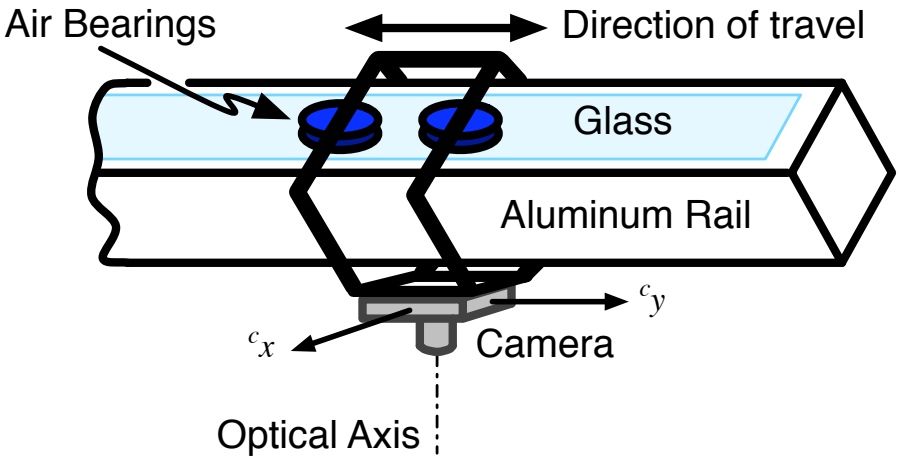

Figure 4-5: Schematic of the camera dolly system.

To minimize the tether load felt by the swimmer, an adjustable boom mounted on the camera dolly extended downward toward the water surface where a clip held the wires at an appropriate distance from the swimmer so as to provide sufficient slack. So long as the camera followed the swimmer, the effects of the tether were found to be minimal.

4.1.3 Resolving Camera Position

In order to resolve the swimmer's position in the inertial frame, it is first necessary to determine the camera's inertial position. Camera motion is constrained to the camera-fixed frame's ${}^{c}y$-axis, shown in Figure 4-5 and runs parallel to the inertial frame's ${}^{i}y$-axis. Evenly-spaced IR LED markers, like those used in the swimmer, were placed along the edge of the tank along its length. As the camera followed the swimmer, at least one LED is always visible at the edge of each frame. The camera's position may be extracted by tracking the LED displacement when processing the recorded image sequences using methods similar to those used to extract the kinematics of the fish itself. Since the tank markers are only visible at the edge of each frame, there was no risk of confusion as to whether a marker belonged to the swimmer or to the tank.

4.2 Pilot Interface

To enable real-time control of the swimmer during experiments, a pilot interface was devised by modifying an off-the-shelf USB gamepad. As seen in the schematic representation in Figure 4-6, the pilot interface boasts a number of analog inputs in the form of two multi-axis potentiometers – one to vary the tail beat amplitude and bias, and one for pectoral fin collective pitch and one for pectoral fin differential pitch – and a sliding potentiometer to adjust the tail beat frequency. Two momentary trigger switches are located on the underside of the pilot interface housing, one of which enables the active markers located on the swimmer when held down. The

second momentary switch, labeled as "Power Trigger" in Figure 4-6, serves as a normally open kill switch for the servo power supply. This control configuration allows an operator to easily manipulate the input parameters with little or no prior experience in piloting devices utilizing flapping foil propulsion, which are still a rarity.

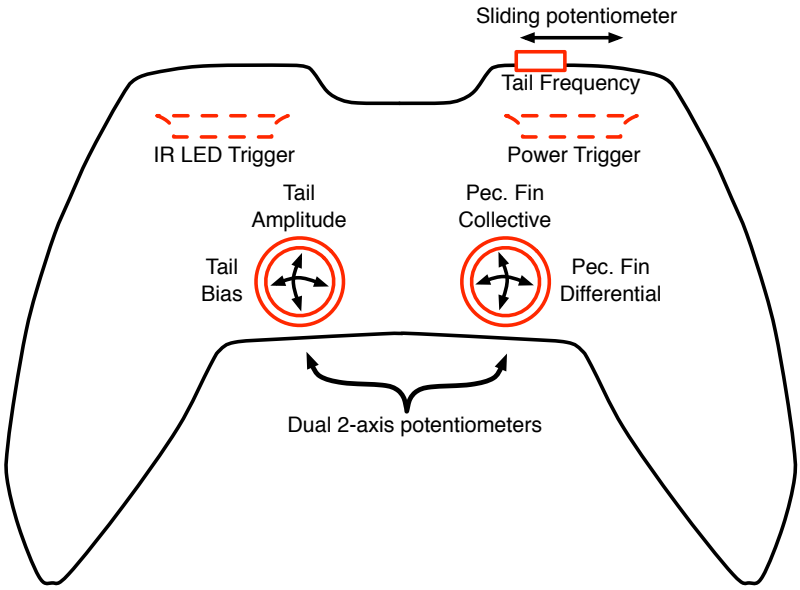

Figure 4-6: Illustration of the swimmer's pilot interface.

For planar motion analysis, the pectoral fin differential and collective pitch controls were not required since the swimmer was trimmed with enough positive buoyancy to provide high roll and pitch stability.

4.3 Input Interpreter

An Atmel®32-bit ARM7 microcontroller (AT91SAM7X256) was programmed to interpret the analog input signals generated by the pilot interface and generate appropriate pulse-width modulation (PWM) output signals that were fed to the tail and pectoral fin servos. A bank of identical low-pass antialiasing filters, were situated between the pilot interface and the microcontroller's analog-to-digital (A/D) converters. A simplified schematic of the input signal flow is provided in Figure 4-7.

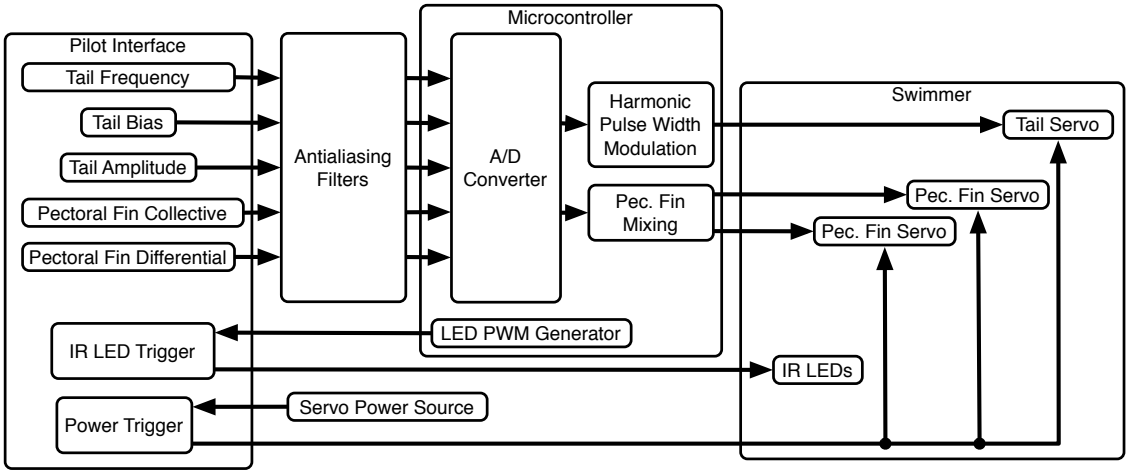

Figure 4-7: Input signal flow schematic.

Each servomotor's angular position was proportional to the pulse width, so by manipulating the duty cycle one could manipulate the servo's position. For the tail servo, the microcontroller used a look-up vector to generate a PWM signal with a sinusoidally varying duty cycle. The sampled DC analog signals from the pilot interface were used to modify various aspects of the stored discretized sine wave period.

The frequency slider varied how long the microcontroller paused before moving to the next element in the look-up vector. When the end of the vector was reached, corresponding to the end of the sine wave period, the code wrapped back around to the first element of the look-up vector.

The digitized tail amplitude signal served as a scaling factor for the look-up vector values, thus its effect was equivalent to scaling the amplitude of a sine wave.

The tail bias signal added an offset to the output signal's duty cycle. This had the effect of shifting the center position about which the tail servo oscillated, allowing for thrust vectoring.

Unlike the tail inputs, the pectoral fin inputs were not parametrically mapped to a stored waveform. Changes to the collective input signal caused both pectoral fin servos to rotate in the same direction to produce a change in body pitch, which may be used for climbing and diving maneuvers.

The pectoral fin differential input caused changes in only one of the pectoral fin's angular positions. The resulting fin asymmetry may be used to induce rolling motions for moderate differential angles. Drag asymmetry may be exploited to increase yaw rates for sharp turns by commanding only one of the pectoral fins to undergo a large deflection.

4.4 Swimmer Prototype

This section discusses the details surrounding the design of the thunniform swimmer that was used to obtain the experimental results presented in Chapter 5.

4.4.1 Material

The swimmer was fabricated by means of a mould casting process. Liquid silicone rubber (Smooth-On®Ecoflex 00-10), the material comprising the bulk of the swimmer, was poured into a two-part wax mould and allowed to cure. The silicone rubber was selected based on its success as a tail material in previous experiments [47, 49]. Unlike the present work, a softer and less viscous silicone gel was previously used for the portion of the body anterior of the tail plate. However, as mentioned in Section 2.1.2, the anterior portion of true thunniform swimmers undergoes little-to-no deformation relative to the body-fixed reference frame while swimming. This observation negates the need for a compliant anterior section. Furthermore, while exploring materials for the present work, the soft, silicone gel used for previous swimmers was found to be easily torn. This characteristic is poorly suited for sealing mechanical connections like the revolute joints for the pectoral fins. Considering the aforementioned items, the swimmer was completely cast from Ecoflex 00-10 silicone rubber.

Results have suggested [47] that the addition of pigment to the silicone rubber changes the cured material's viscoelastic properties. The addition of yellow pigment (1% by mass) was found to provide the desired balance between material density ρ, stiffness E and viscosity μ for producing thunniform style swimming motions.

4.4.2 Internal Components

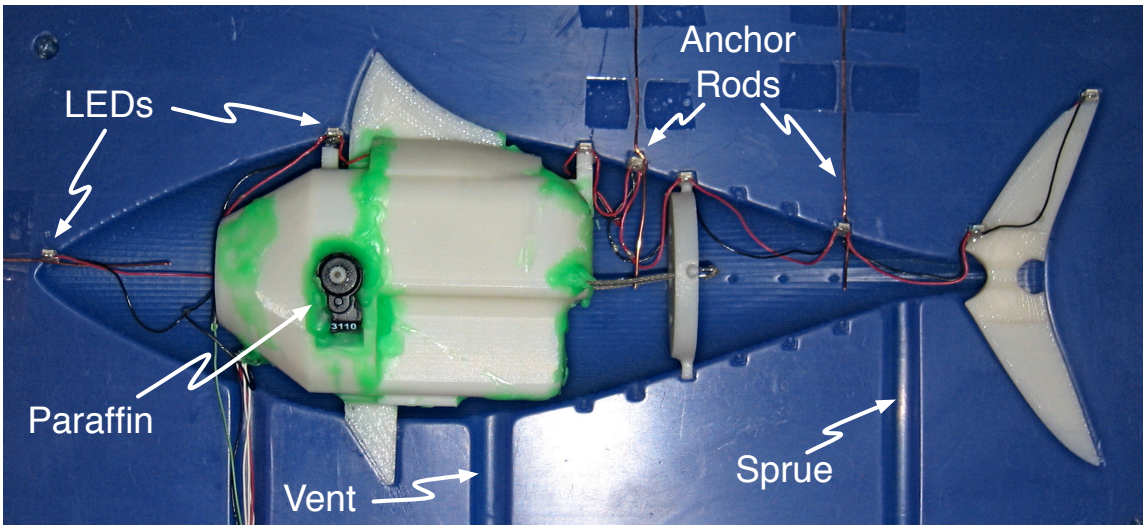

Figure 4-8: Mould and part preparation prior to casting.

A handful of rigid components are encased in the silicone rubber body, as shown in Figure 4-8. The caudal fin, tail plate, dorsal fin, actuation module, along with the pectoral fins (not shown) were fabricated using a Dimension 3-D printer. The printed parts have material properties consistent with those of ABS thermoplastic.

Since the biomimetic swimmer has adopted a pelagic morphology, the caudal fin is homocercal and contain a rigid core, so there is no negative pitching moment is produced or needed since the anterior body is symmetric about the lateral plane. The geometric design of the aforementioned rigid core follows aeronautical conventions for lifting surfaces. The cross-sectional shape is a symmetric foil. The sweep-back angle λ, span b, root chord c_r and tip chord c_t are based on those of the of Yellowfin Tuna (*Thunnus albacares*).

The primary purpose of the actuation module is to contain the single tail and two pectoral fin servo motors. A stock Hitec®HSR-5995TG digital servo actuates the tail plate via a pair of vinyl coated stainless steel cables, measuring 0.95 mm in diameter. The cables were coated with PTFE heat-shrink tubing to reduce friction where they exited through small holes at the rear of the actuator module. A pair of Futaba®S3110 miniature servos were selected to both actuate and support the pectoral fins.

The tail plate is the means by which the actuator interfaces with the swimmer's tail. A drawing of the tail actuation system can be seen in Figure 4-9. The two stainless steel cables affixed to the ends of the tail servo's horn pass through the tail plate and are terminated using cable crimps. As the servo horn rotates in either direction, the tension in either steel cable forces the plate to both rotate and translate, although the former is more prominent.

The dual cable mechanism for actuating the tail is not too distant from the muscle configuration found in real thunniform swimmers. Figure 4-10 illustrates the two powerful bundles of red muscle that responsible for propelling warm bodied fish at high speeds. Muscles are only capable of generating force through contraction, so to produce oscillatory tail motions required for swimming, the bundles contract in an alternating manner.

Previous compliant swimmers of similar design were plagued by weight issues, making them negatively buoyant. A number of simple, yet effective choices were made during the current prototype's design to produce a device that did not sink. An anterior

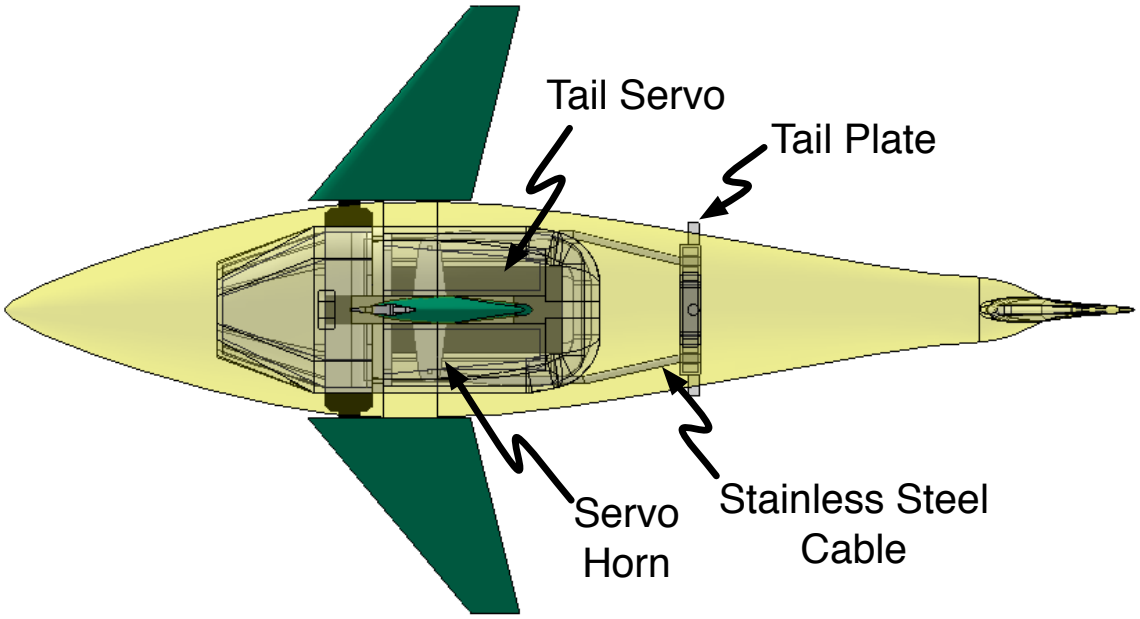

Figure 4-9: Dorsal perspective illustration of the prototype indicating tail actuation components.

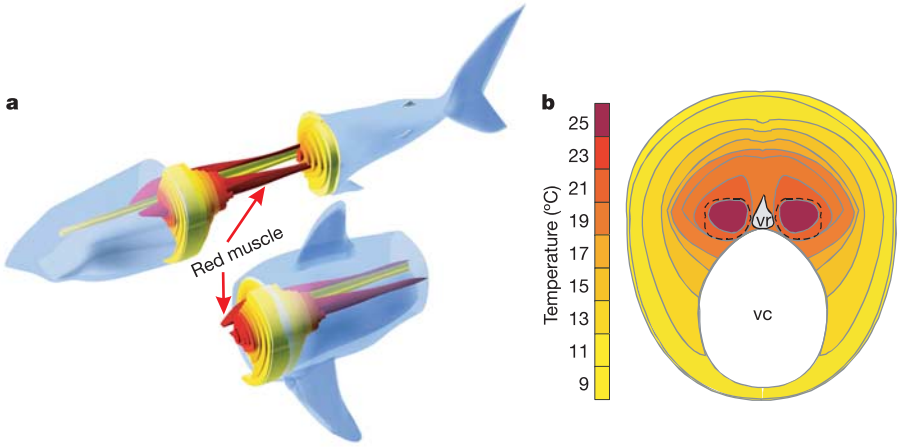

Figure 4-10: Red and white muscle temperature distributions in salmon sharks (*Lamna ditropis*): (a) isotherms indicating the two long bundles of red muscle responsible for moving the tail; (b) body section just anterior of dorsal fin. Abbreviations: vc, visceral mass; vr, vertebrae. From [6].

buoyancy chamber augmented the buoyancy provided by the actuation module's air space. The chamber also housed the main wiring harness and a large electrolytic capacitor, to assist in powering the tail servo during peak loads. Although the chamber reduced the body's forward compliance, the body-relative anterior dynamics of previous swimmers were observed to be of little significance in terms of affecting their overall swimming capabilities. Lastly, the tail plate and pectoral fins were designed and fabricated as hollow parts to help reduce the swimmer's material weight.

As is also evident from Figure 4-8, the IR LEDs used for the active markers are temporarily fixed in place in one half of the mould prior to casting. To prevent the markers from becoming dislodged after casting, the LEDs were either mounted on rigid internal components atop copper wire segments, or anchor rods, using a clear epoxy resin. To minimize the impact on body dynamics, the anchor rods were positioned with their axes in the ${}^{b}z$-direction. Epoxy was also used to encase the marker electrical connections to safeguard against electrical shorts.

To help protect the internal electronics from leaks during both the casting process and while swimming, all of the actuation module's seams were joined with CA adhesive and sealed with melted paraffin which is both buoyant and compatible with the Ecoflex rubber. The paraffin is the bright-green material visible in Figure 4-8.

Immediately after casting, the swimmer was completely sealed from the environment with the exception of the dorsal, ventral, and pectoral fin joints. A desirable feature of the silicone rubber was its ability to bond to previously cured material. Taking advantage of this characteristic, silicone rubber was manually brushed onto the aforementioned surfaces and joints. A close-up photograph of the left pectoral fin joint is included in Figure 4-11. The cured silicone rubber sleeve was flexible enough

to permit the servo horn to easily rotate without tearing.

Figure 4-11: Sealed pectoral fin joint. The leading edge is towards the left.

Figures 4-12 through 4-14 contain pictures of the completed prototype. Characteristic dimensions are provided in Table 4.1.

Body		
Length, ℓ		m
Maximum girth	0.195	BL
Maximum height	0.27	BL
Tail plate position, ${}^{b}x_{TP}$	0.227	BL
Mass, m_b	0.325	kg

Tail		
Foil	NACA 0030	-
Span, b_T	0.353	BL
Aspect ratio, $\mathcal{R}_T$	7.2	-
Taper ratio, λ_T	0.24	-
Root chord, c_{r_T}	0.08	BL
Mean hydrodynamic chord, $\bar{c}_T$	0.0552	BL
Mean hydrodynamic center, ${}^{b}x_{\bar{c}_T}$	-0.55	BL
Leading edge sweep, Λ_{LE_T}	35	$^\circ$

Pectoral Fins		
Foil	NACA 0021	-
Span, b_{PF}	0.54	BL
Aspect ratio, $\mathcal{R}_{PF}$	5.8	-
Taper ratio, λ_{PF}	0.3	-
Root chord (at servo joint), $c_{r_{PF}}$	0.144	BL
Mean hydrodynamic chord, $\bar{c}_{PF}$	0.1024	BL
Mean hydrodynamic center, $\left({}^{b}x_{\bar{c}_{PF}}, {}^{b}y_{\bar{c}_{PF}}\right)$	$(0.16, \pm 0.11)$	BL
Leading edge sweep, $\Lambda_{LE_{PF}}$	40	$^\circ$

Table 4.1: Prototype swimmer characteristic dimensions.

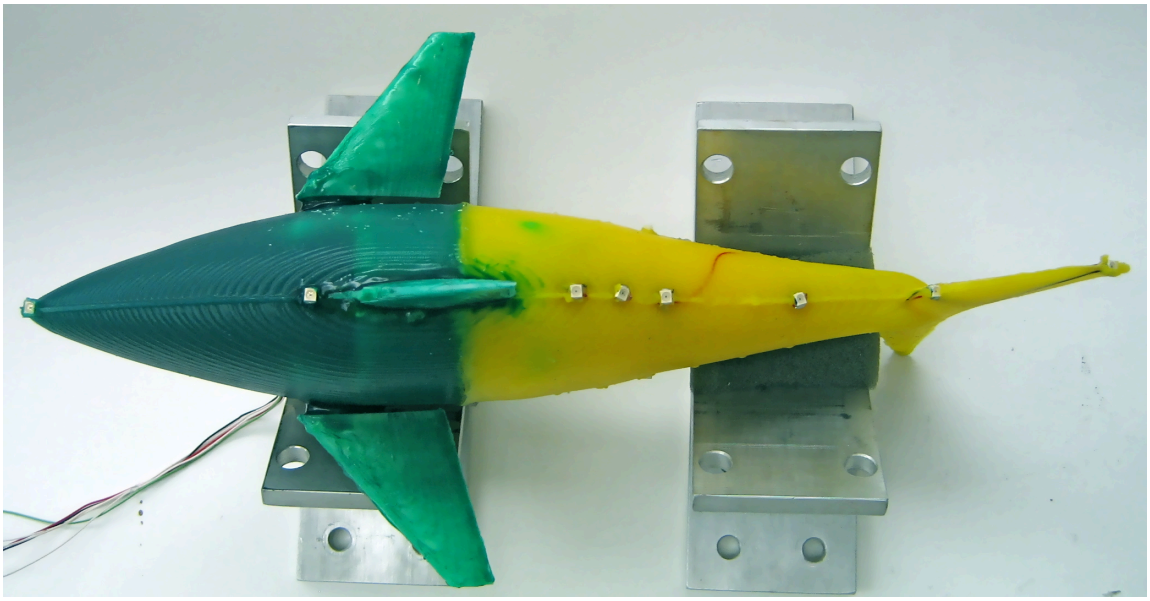

Figure 4-12: Dorsal view of the completed swimmer, affectionately named McMaster-Carp on account of its green and yellow colour scheme resembling that of the McMaster-Carr Supply Company®.

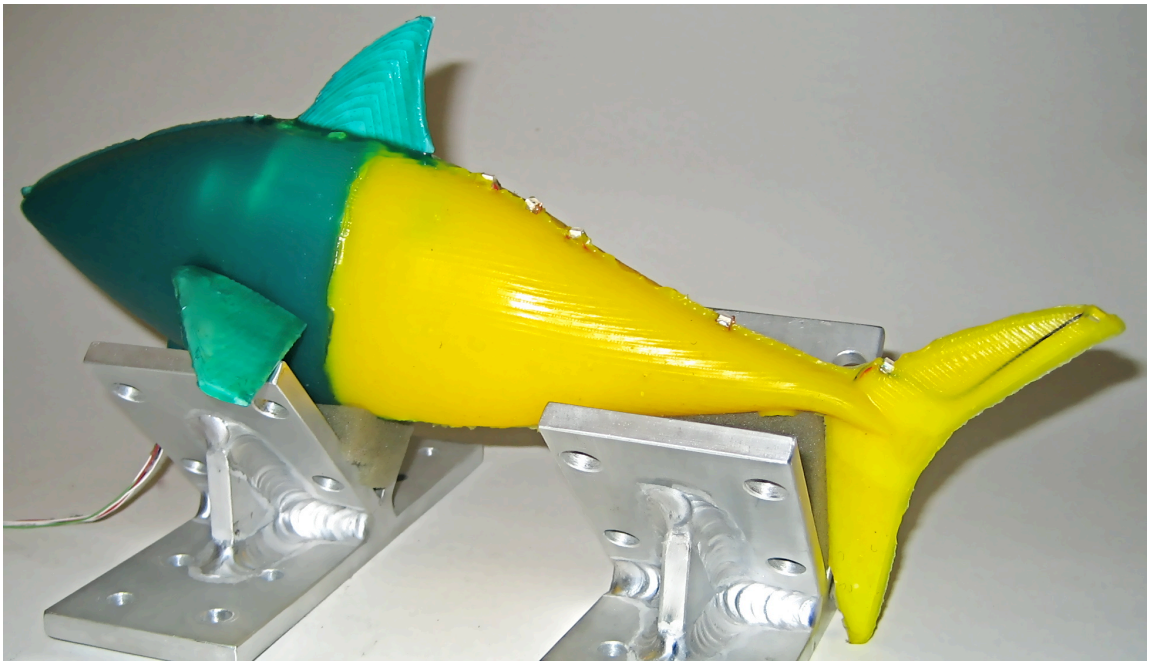

Figure 4-13: Posterolateral view of completed swimmer.

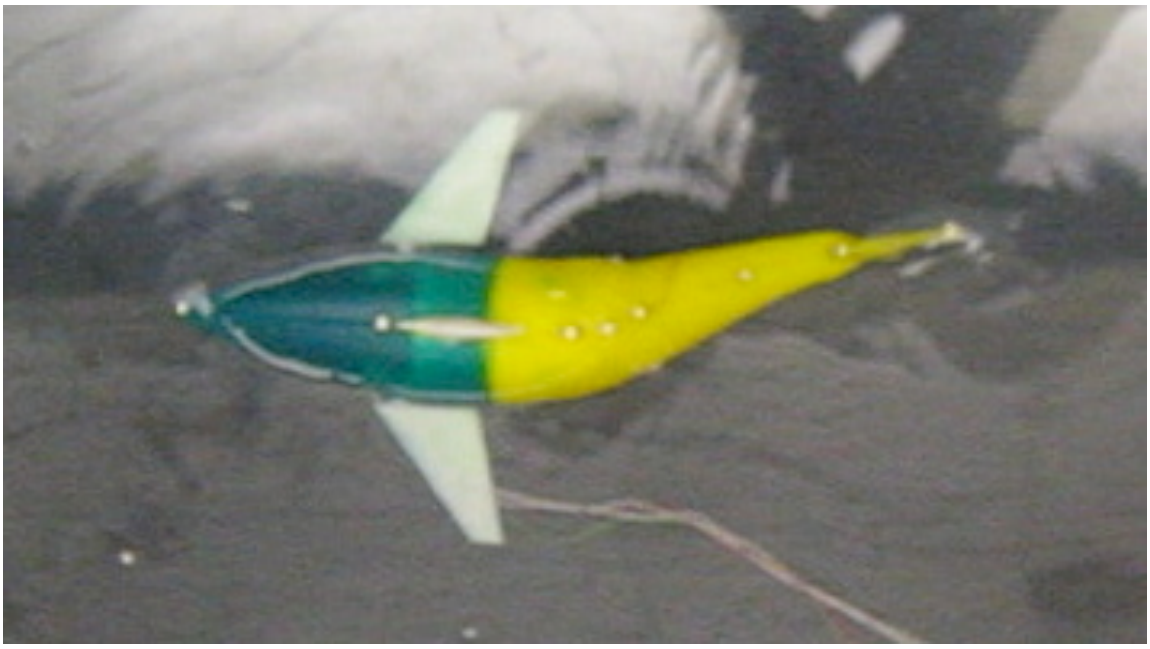

Figure 4-14: Swimming prior to final joint sealing.

Chapter 5

Analysis of Experimental Results

We now consider the processing of experimental results obtained using the apparatus described in Chapter 4. Kinematic data from experiments will be discussed and compared with those from a model-based simulation.

5.1 Preprocessing

Optical systems are affected by various types of spatial distortion. For the case of the motion-capture system that was devised for this work, most of the distortion was caused by the camera lens in the form of both radial and tangential components. In short, the spatial distortion will typically cause straight lines to appear curved, especially near the edges of an image. To extract meaningful kinematic data from recorded frames, it was necessary to characterize the camera system's distortion and

correct each frame using an optical distortion model that was determined using a camera calibration procedure. The model and results are provided in Appendix A.

After compensating for spatial distortion, each 8-bit grayscale frame was binarized using Otsu's method [33], which automatically performs thresholding based on an image's intensity histogram. The resulting 1-bit black-and-white images were scanned for contiguous regions of white pixels, or blobs, which correspond to the individual markers. The negative of a single frame is shown in Figure 5-1a.

The tank-mounted markers used to track the camera position were known *a priori* to reside within a fixed margin of pixels along the right-hand side of each frame, indicated in Figure 5-1b. For each frame, this portion was processed separately from the rest of the image, which will be referred to as the cropped frame.

In each cropped frame, the marker blob centroids were computed in pixel coordinates. It was observed that the marker LEDs produced a fairly Gaussian intensity profile, justifying the assumption that the center of each image blob corresponded to the center of a physical marker. Due to the highly effective optical filtering, there were no ambiguities present in any of the frames so it was not necessary to perform any further filtering in software. The computed centroids were ordered based on their center-to-center pixel distances. Using this method, the rough orientation of the swimmer could be identified since the anterior markers were known to be physically further apart than the markers near the posterior of the swimmer. The sorted marker numbering scheme is shown in Figure 5-1c, note that marker 1 corresponds to the nose of the swimmer, markers 2 and 3 are fixed to the actuation module, marker 5 is atop the tail plate, and markers 7 and 8 sit at the root and tip of the caudal fin,

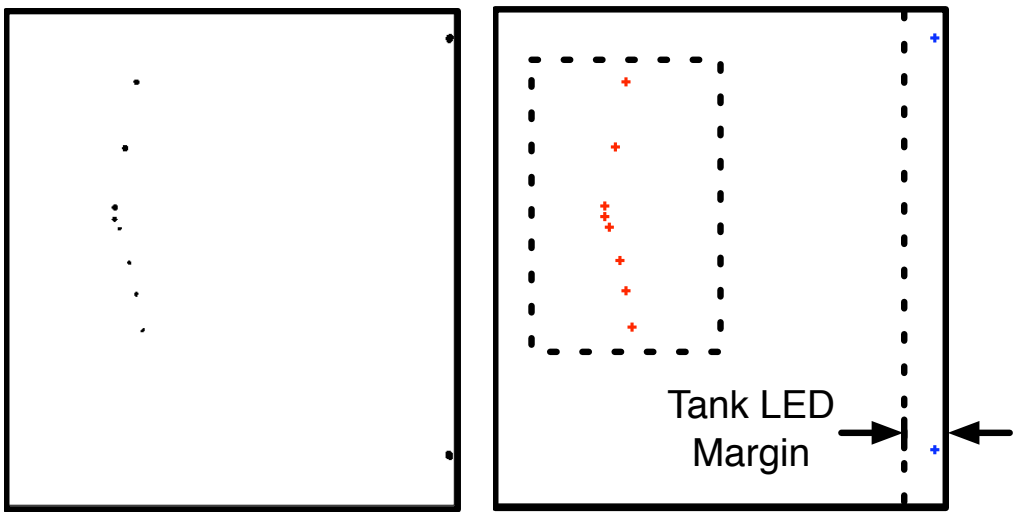

(a) Binarized frame.

(b) Detected swimmer and tank markers.

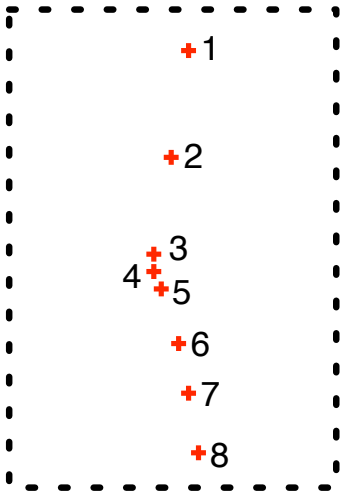

(c) Labeled markers.

Figure 5-1: Key steps in marker identification.

respectively.

The margin of pixels containing the tank markers was handled in a similar manner to the cropped frame. The markers were spaced such that each frame was known to contain at least one marker. As the camera followed the swimmer, the markers would enter the field of view through the top of the frame and exit via the bottom. Whenever a marker's coordinates were within a specified margin of pixels near the bottom of the frame, it was considered to be exiting and the algorithm's focus shifted to tracking the position of the second visible marker, located near the top of the frame. The resulting time series for the camera position resembled a sawtooth wave and was subsequently unwrapped to produce a continuous time record trace of the camera's position throughout a given experiment.

It was found that while recording, the camera or computer would occasionally drop a frame, which resulted in gaps in both the swimmer and camera position data records. An automated procedure was devised to identify missing frames and estimate the missing marker coordinates using cubic spline interpolants.

To attenuate high frequency jitter of the marker coordinates, local smoothing of each data record was carried out using suitable Savitzky-Golay polynomial filters [19].

The final preprocessing step was to convert the image-based measurements to physical units. The coordinates of the swimmer and camera markers were linearly scaled from pixels to meters, and the frame numbers to seconds. The scale factor was deduced by measuring the distance in pixels between markers 2 and 3, whose physical distance was known.

5.2 Extracting Kinematics: A picture is worth 640×480 words

An outline of the procedure for extracting and estimating both the swimmer and camera kinematics is presented below. Illustrative results based on experimental data are included.

5.2.1 Body Orientation

The orientation of the body-fixed frame within the camera coordinate system was computed by finding the direction of a vector from marker 3 to marker 2. These markers were especially well-suited for this purpose since they were positioned on a rigid portion of the body that also contains the center of mass. The position of the body-fixed frame relative to the camera origin O_c was computed using the coordinates of marker 3, which was defined to be O_b.

Figure 5-2 shows a plot of the swimmer's body orientation, or heading angle ψ, relative to both Σ_i and Σ_c. Starting from a state of rest, one may observe how the amplitude decreases as the swimmer gains speed and its body stabilizes. The four anomalous peaks (two at 17 seconds and two at 25 seconds) are due to pilot applied tail biases that were required to prevent the swimmer from colliding with the tank walls.

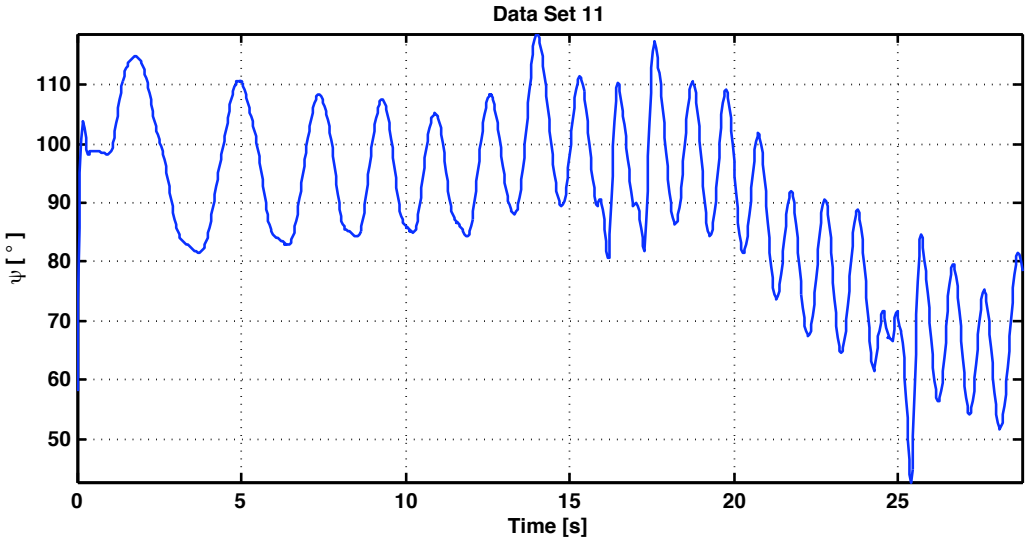

Figure 5-2: Body heading angle with respect to Σ_i and Σ_c.

5.2.2 Body-relative Kinematics

Since the recorded frame sequences only provide position data, numerical differentiation was used to compute marker velocities and accelerations. Since differentiation is inherently a noise amplifying operation, Savitzky-Golay differentiation filters were used to compute the position data's first and second time derivatives. This conditioning allowed pertinent high-frequency signal content to be retained whilst attenuating noise.

The longitudinal and lateral displacements, velocities, and accelerations of the swimmer's markers relative to the Σ_b are shown in Figures 5-3 through 5-5. The presented time series plots depict the swimmer starting from rest and reaching a steady swimming state. At steady state, the lateral deflection amplitudes for each marker are

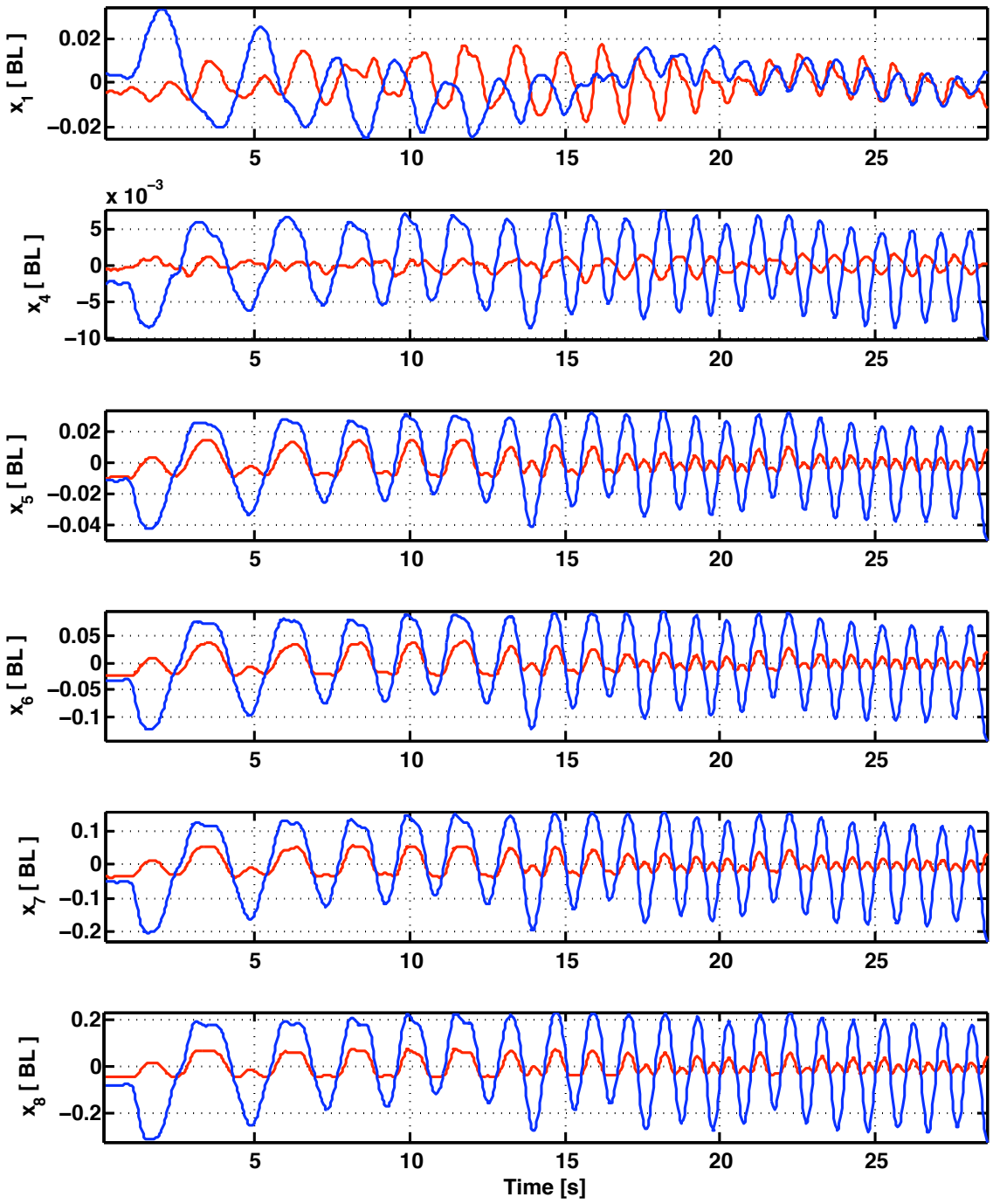

Figure 5-3: Extracted marker displacements with respect to body frame; (—) ${}^{b}x_k$, (—) ${}^{b}y_k$, $k = 1, 4, 5, 6, 7, 8$. Values normalized by characteristic length ℓ.

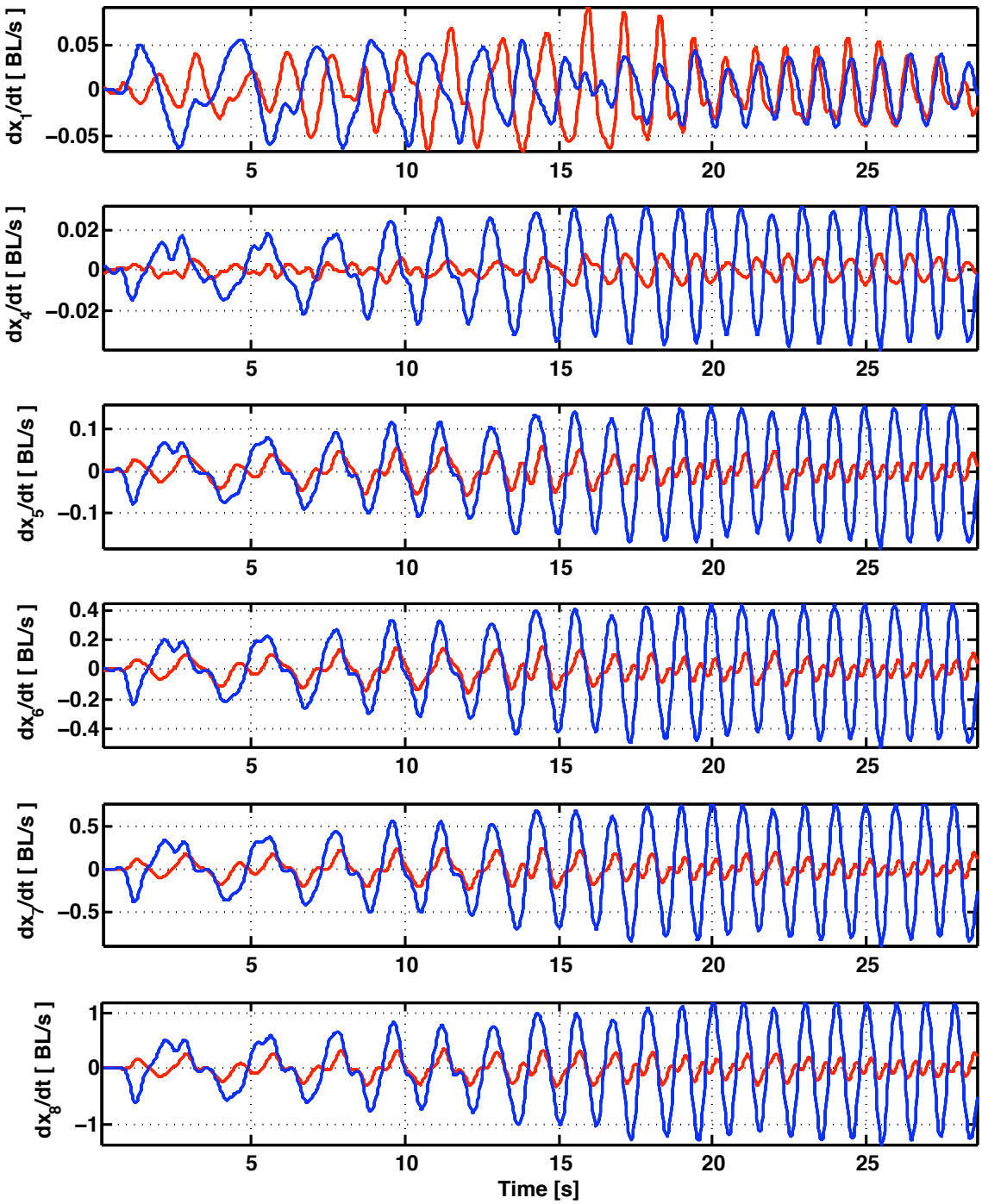

Figure 5-4: Extracted marker velocities with respect to body frame; (—) ${}^b\dot{x}_k$, (—) ${}^b\dot{y}_k$, $k = 1, 4, 5, 6, 7, 8$. Values normalized by characteristic length ℓ.

consistent with the trends published by Videler [50] for a steadily swimming saithe.

5.2.3 Estimating Body Segment Rotation

The primary source of excitation to the swimmer is the angular deflection of the actuator-driven tail plate ${}^b\theta_5$. Since only a single row of dorsal markers ran along the length of the swimmer, one cannot directly measure the angular rotation of a given body segment relative to the undeformed body centerline. Frame-by frame, cubic splines were fitted to both the anterior and posterior portions of the body using the marker coordinates as knots. For reference, an example of one of the instantaneous spline fits is provided in Figure 5-6.

The anterior spline spanned the section of the swimmer between markers 1 and 2. A natural boundary condition was assigned to the knot at marker 1, and fixed boundary condition at the marker 2 knot, since the latter is connected to the rigid actuation module, which in turn, is fixed to the ${}^b x$-axis.

The posterior spline fit included the portion of the body between markers 3 and 7. Like marker 2, the knot at marker 3 was assigned a fixed boundary condition as it was coincident with O_b. Because of the the caudal fin's rigid plastic insert, the orientation, or pitch angle, of the caudal fin could be determined from the direction of a vector from marker 8 to marker 7. When computed with respect to Σ_b, the caudal fin's pitch angle ${}^b\theta_{CF}$ served as the boundary condition at the marker 7 knot. Figure 5-7 presents a plot of the caudal fin pitch angle during one of the swimming

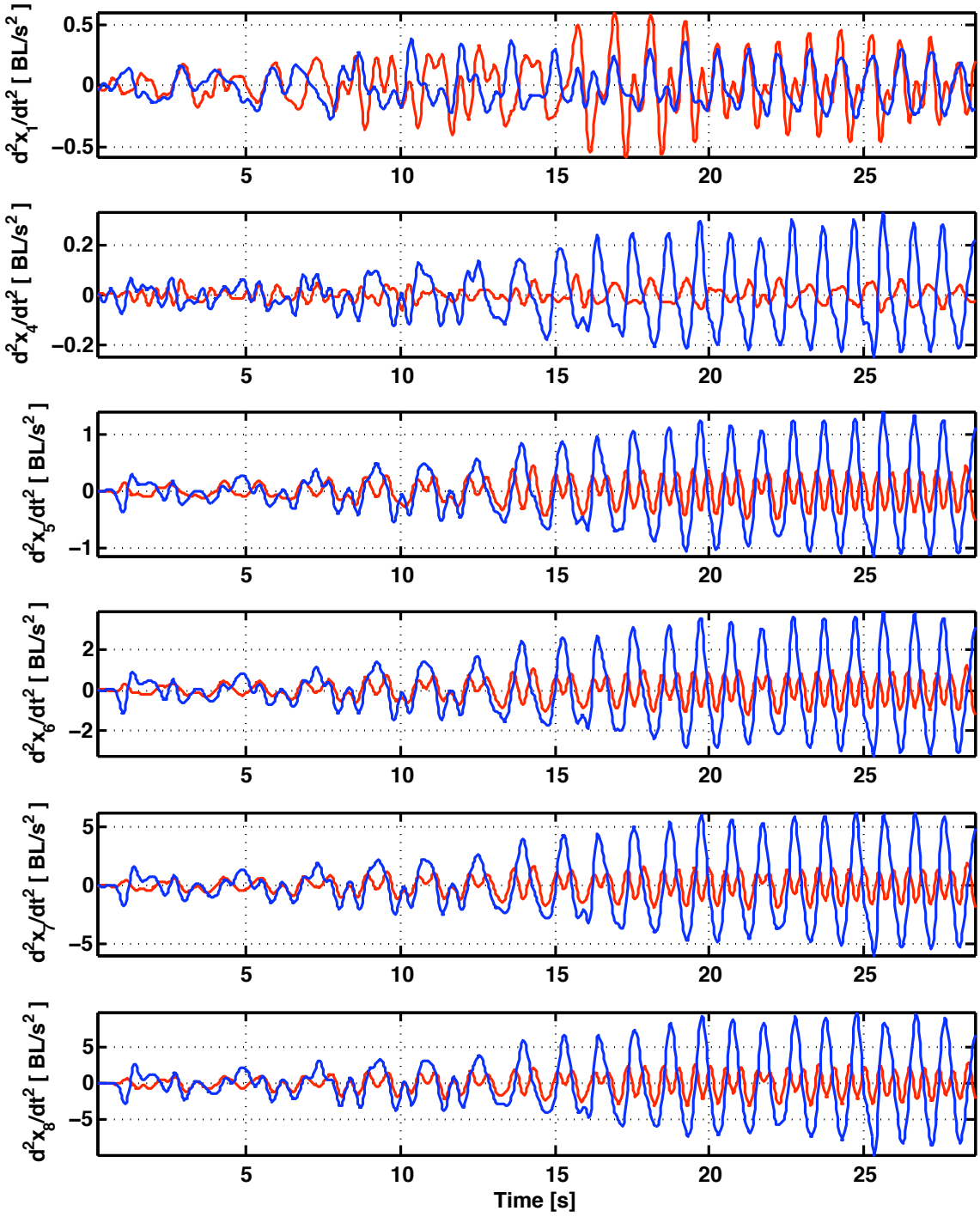

Figure 5-5: Extracted marker accelerations with respect to body frame; (—) ${}^b\ddot{x}_k$, (—) ${}^b\ddot{y}_k$, $k = 1, 4, 5, 6, 7, 8$. Values normalized by characteristic length ℓ.

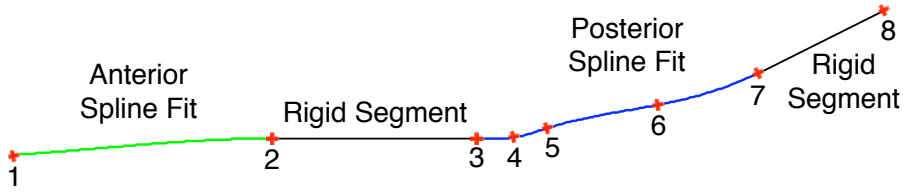

Figure 5-6: Anterior (green) and posterior (blue) spline fits.

experiments. Markers 4 through 6 were used as intermediate knots to guide the spline fit.

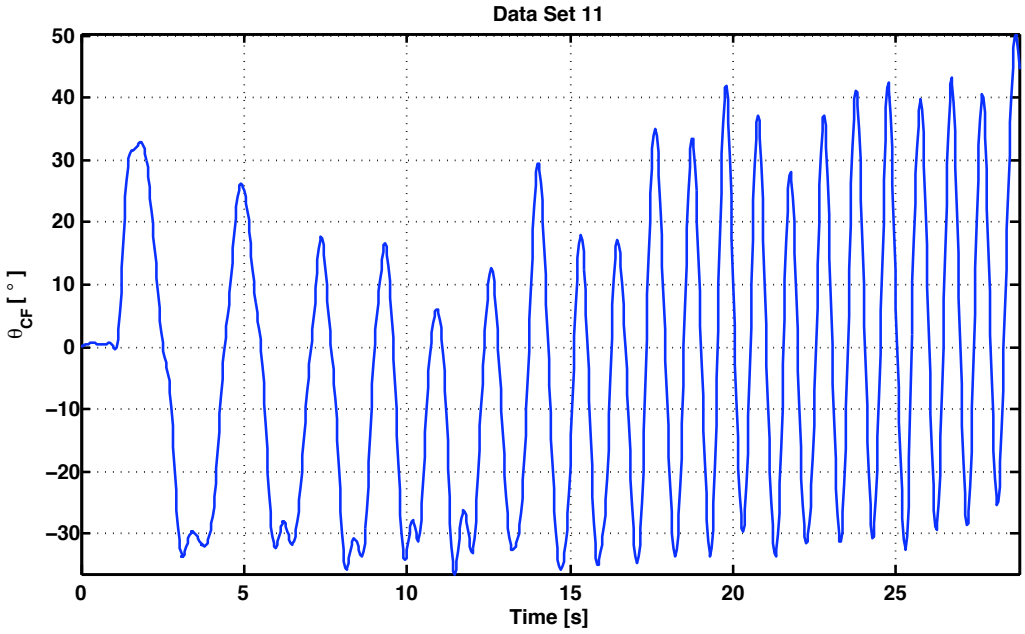

Figure 5-7: Time series plot of caudal fin pitch angles.

By overlaying all of the computed splines from one experiment, it is possible to construct a qualitative description of the swimmer's kinematic envelope. Such a plot is shown in Figure 5-8 for steady-state swimming conditions.

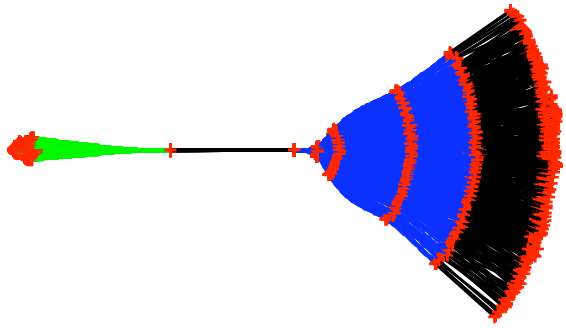

Figure 5-8: Composite plot of spline kinematics with respect to the body-fixed frame during steady state swimming.

From the spline fits, the position and slope of any point on the swimmer may be estimated. The slope, and thus the deflection angle ${}^{b}\theta_{TP}$ and normal direction, of the tail plate were computed by differentiating the spline fit with respect to ${}^{b}x$ at the marker 5 knot position. An example plot depicting the computed tail plate angular deflection time series is shown in Figure 5-9.

5.2.4 Camera Kinematics

Since the observation frame Σ_c is free to move relative to Σ_i, the camera's kinematics must be estimated as well. As mentioned earlier, the camera dolly constrains the camera's motions to translation in the ${}^{i}y$ (and ${}^{c}y$) direction. A small amount of transverse motion in the ${}^{i}x$ (and ${}^{c}x$) direction is evident from the plots in Figure 5-10, however the perturbations are orders of magnitude smaller than the characteristic length scale ℓ and have negligible effect on the results when transforming the body's kinematics from Σ_c to Σ_i.

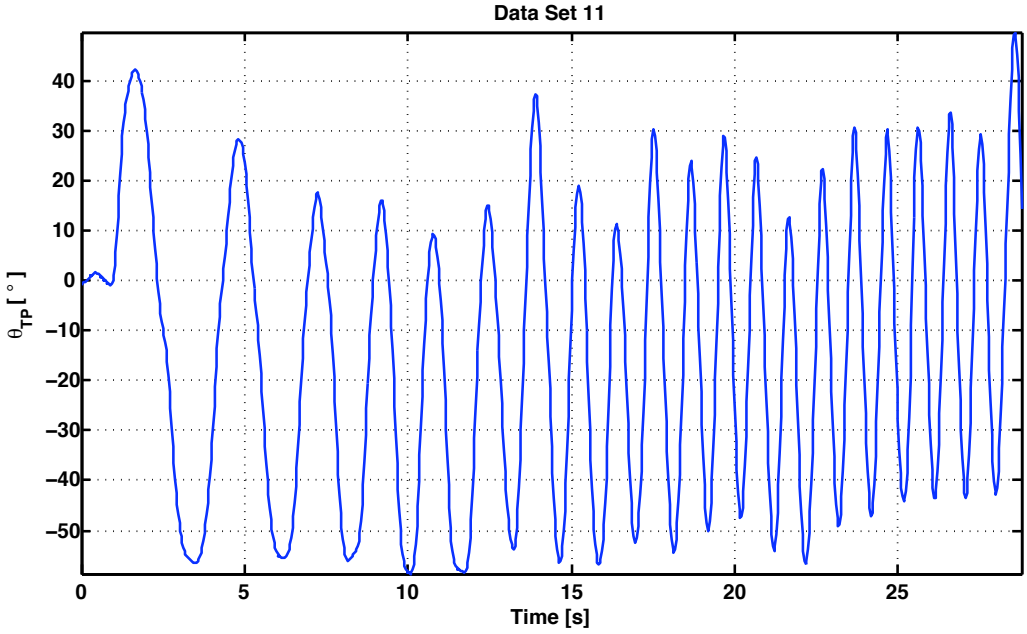

Figure 5-9: Time series of tail plate angular deflections ${}^{b}\theta_{TP}$.

Like the swimmer, the velocity and acceleration of O_c were computed using Savitzky-Golay differentiating filters.

Since the camera dolly is manually towed along the length of the tank there is a certain amount of human-induced noise added to the measured coordinates. Disturbances of this type are exemplified by the anomalies, near 5 seconds and 23 seconds in the velocity and acceleration plots of Figure 5-10. These effects are subtracted when transforming the body kinematics from Σ_c to Σ_i.

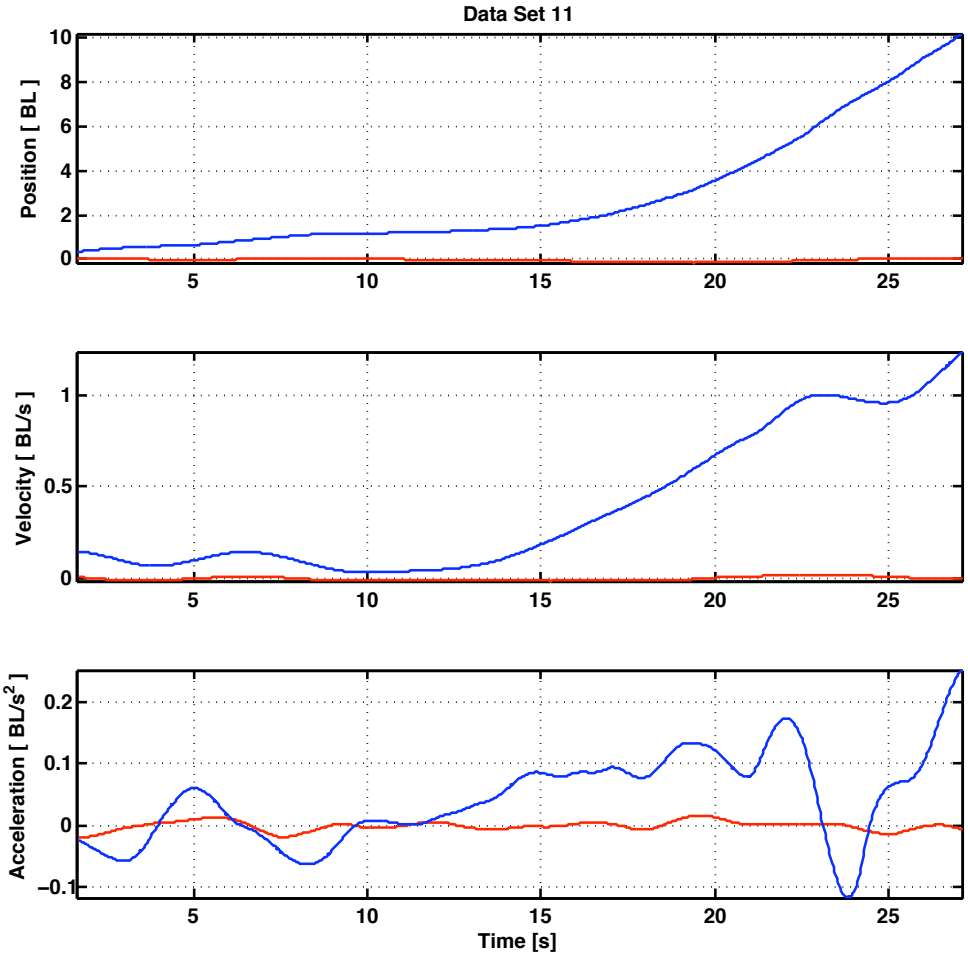

Figure 5-10: Measured camera kinematics with respect to the inertial frame;(—) ${}^{i}x_c, {}^{i}\dot{x}_c, {}^{i}\ddot{x}_c$; (—) ${}^{i}y_c, {}^{i}\dot{y}_c, {}^{i}\ddot{y}_c$. Values normalized by characteristic length ℓ.

5.3 Tail Kinematic Relationships

A number of Volterra series expansions [20] were identified to describe the nonlinear kinematic relationships between the tail plate angular and lateral deflections, θ_{TP} and h_{TP}, and the caudal fin displacements, θ_{CF} and h_{CF}. The tail plate motions were viewed as sources of excitation to the swimmer, which responded by producing caudal fin motions. Different sets of data were used to generate and test the Volterra kernels. Figures 5-11 through 5-14 contain plots of some of the test results comparing the Volterra series estimates of each kinematic relationship with real measured response data.

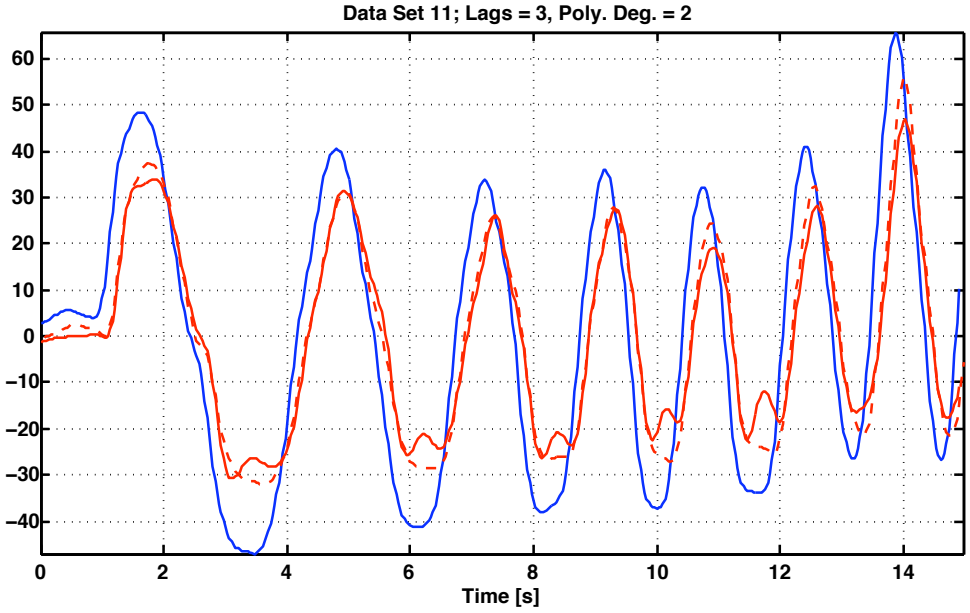

Figure 5-11: Measured (solid) and estimated (dashed) caudal fin pitch angle [°] and measured tail plate angular deflections [°]; (—)θ_{TP}, (—)θ_{CF}.

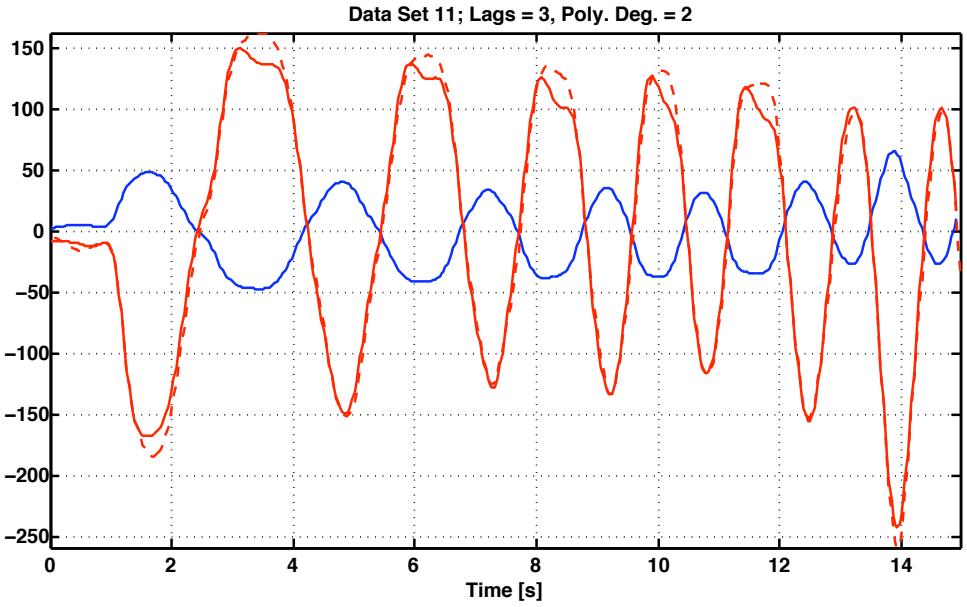

Figure 5-12: Measured (solid) and estimated (dashed) caudal fin lateral displacements [BL$\times 10^3$] and measured tail plate angular deflections [°]; (—)θ_{TP}, (—)h_{CF}.

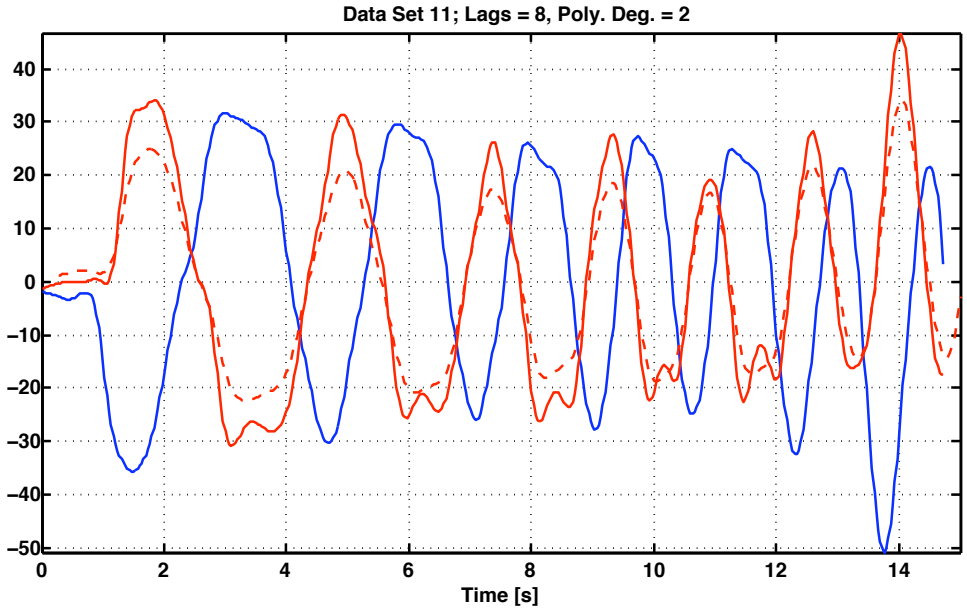

Figure 5-13: Measured (solid) and estimated (dashed) caudal fin pitch angles [°] and measured tail plate lateral displacements [BL$\times 10^3$]; (—)h_{TP}, (—)θ_{CF}.

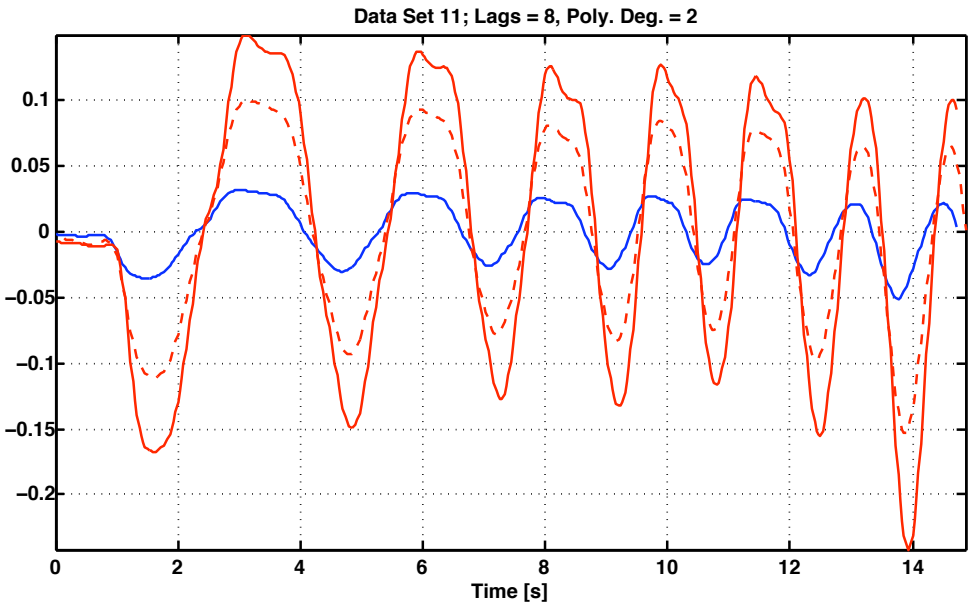

Figure 5-14: Measured (solid) and estimated (dashed) caudal fin lateral displacements [BL$\times 10^3$] and measured tail plate lateral displacements [BL$\times 10^3$]; (—)h_{TP}, (—)h_{CF}.

Figures 5-11 and 5-12 show strong agreement between the measured and estimated caudal fin kinematic variables θ_{CF} and h_{CF}. Increasing both the memory length and order of either series was found to reduce the discrepancies between the measured and estimated response peaks, however in doing so the expansions became unwieldy and computationally expensive. Furthermore, the error seen in the estimated kinematics is well below the margin of error introduced by other sources, namely the hydrodynamic coefficient estimates and the quasi-steady assumption in the tail thrust model.

The phase lag ϕ_T between the caudal fin's heave and pitch motions that was introduced in Section 3.6.2 is most apparent Figures 5-12 and 5-13, where the pitch and heave excitations are respectively out of phase with the heave and pitch responses.

The expansions in which the tail plate lateral displacement h_{TP} was the independent variable, or excitation source, required a many lags before the amplitudes of the estimated response began to converge with the measured response. This is visible in Figures 5-13 and 5-14. This may suggest that both of the caudal fin kinematic variables have a stronger dependancy on the tail plate's angular deflections θ_{TP} than on the lateral deflections h_{TP}.

5.4 Model Validation

The prototype swimmer's geometric and material properties were entered into a parametric model that was designed to simulate the swimmer's dynamics and was based on the principles of Chapter 3. The kinematic relationships of Section 5.3 were used to estimate the caudal fin kinematics for a given set of tail plate motions. The

estimated caudal fin pitch an heave motions were then fed into a flapping foil model along with the body's velocity vectors, ${}^b\boldsymbol{v}_b$ and ${}^b\boldsymbol{\omega}_b$, which were, in turn, fed into the quasi-steady lift model of Section 3.6.3. Once the estimated lift and drag relative to the caudal fin-fixed frame were computed, they were projected onto the body axes from the caudal fin axes, producing body-relative force and moment estimates. A block-diagram representation of the tail thrust model is shown in Figure 5-15.

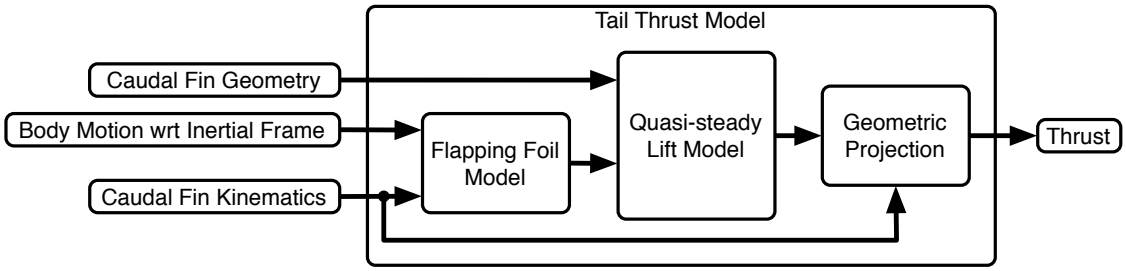

Figure 5-15: Data flow used by the kinematics-based thrust model.

To help ensure validity, the model states were initialized using real data values from a data record that was not used to compute the Volterra kernels. The average tail beat frequency, longitudinal velocity, and tail beat amplitude were $\omega_T = 2\pi\,(0.85)$ rad/s, $u = 0.055$ m/s, and $H_{To} = 0.0273$ m resulting in a Strouhal number of $St = 2.65$. Similarly, the Reynolds number was approximately $Re_\ell = 14600$, placing it in an appropriate flow regime for the drag models of Chapter 3. As a point of reference, Strouhal numbers between 0.25 and 0.35 are considered to be indicative of efficient swimming motions [46], this suggests that the prototype was moving much too slowly given its tail beat frequency and amplitude. Valdivia's results for similar compliant swimmers [47] suggest that the tail beat frequency should in fact be higher for increased propulsive efficiency. Unfortunately, the tail servo was designed for high

torque not high speed, and higher tail beat frequencies could not be achieved without reducing the tail beat amplitude.

Simulation results are provided in Figure 5-16. Comparing the simulated results with the experimental ones, it is evident that the model overestimates the damping and inertial characteristics of the swimmer, resulting in additional low-pass dynamics. This likely the result of overestimates for the body drag or added mass coefficients. Nonetheless, there is a strong correlation between the trends shown by the model and prototype states.

As an aside, the pilot interface with its analog inputs, was an enabling feature. While not quantitatively measured, it was discovered that the prototype swimmer was capable of swimming in a full circle within the confines of its 0.6 m wide tank. The resulted in a turning radius of about one body length. This feat was only accomplished because of the ability to provide continuous pilot inputs, versus keyboard commands, a first for this type of swimmer.

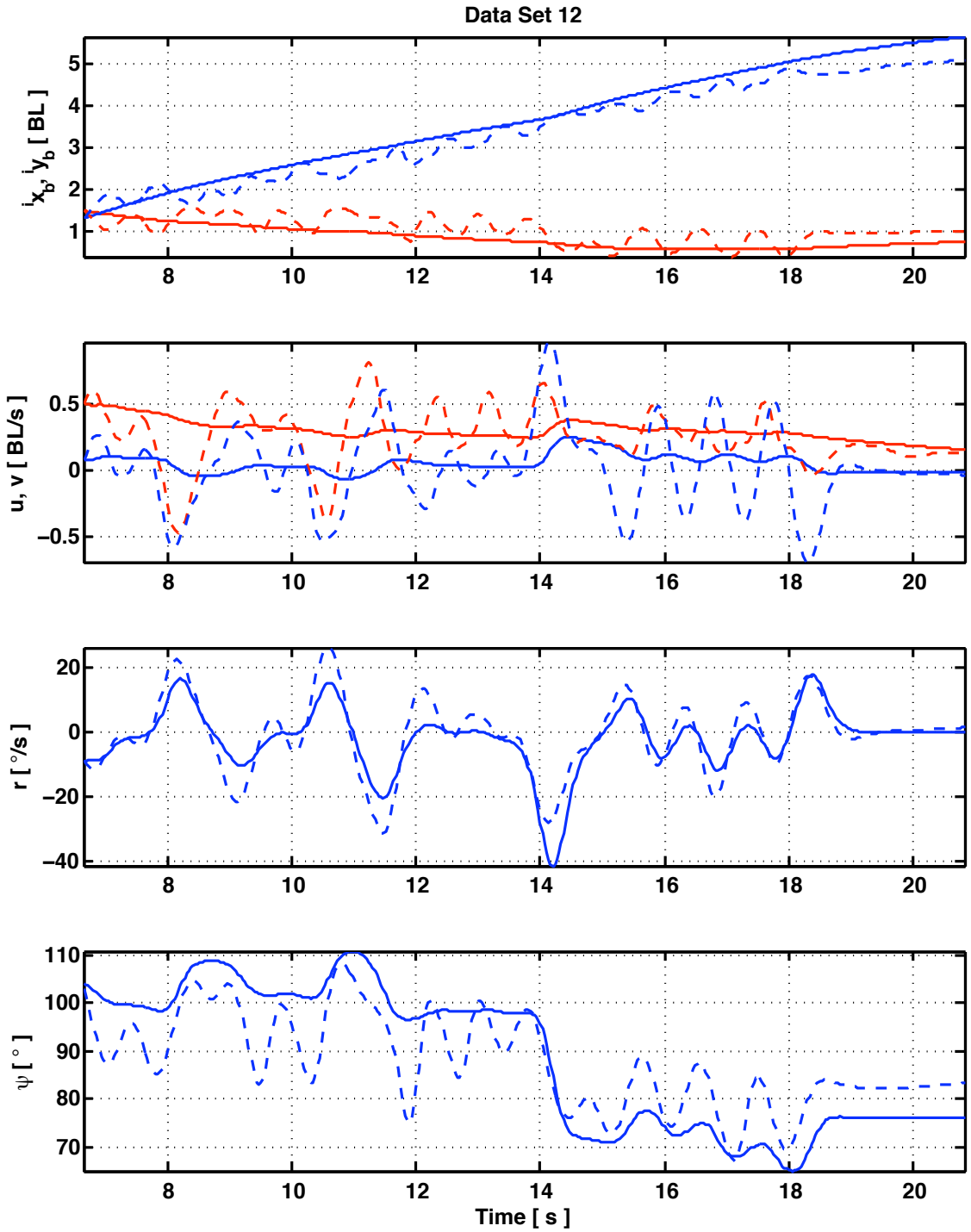

Figure 5-16: Simulated (solid) and experimental (dashed) results; (—) $^i x_b, u$; (—) $^i y_b, v, r, \psi$. The flat portion in the plots starting at around 19 seconds is the swimmer coasting without any control inputs.

Chapter 6

Conclusions and Closing Remarks

6.1 Thesis Summary and Contributions

A short overview of fish morphology was provided as a basis for later commentary on biological design elements. An abridged literature survey on modeling of swimming fish, flapping foil propulsion, and fish-like devices was presented to help motivate the topics of discussion found in the subsequent chapters.

An alternative modeling methodology based on engineering primitives and emphasizing practicality was proposed and later implemented. Rigid body kinematics and dynamics with respect to various coordinate systems were described as a prelude to the following sections, which discussed the hydrodynamic interactions between the body and the surrounding fluid. Practical models for added mass and fluid dynamic drag due to the swimmer's body were discussed. Elements for the caudal fin thrust

model were explored, including flapping foil kinematics and dynamics. The pectoral fin load decomposition was illustrated prior to assembling the full set of dynamic equations.

An accessible, inexpensive means of reliably measuring the kinematics of a submerged swimmer was devised. Most studies on swimmer kinematics, including previous work with the compliant swimmers, required manual selection of two or three body points on a frame-by-frame basis, producing low fidelity kinematics with high variance. The frame processing method used in this work was completely automated, ensuring repeatability and consistency.

A minimal number of steps for preprocessing the recorded frames was found to included removal of spatial distortion, binarization, blob detection, coordinate sorting, dimension scaling, and local smoothing in the time domain.

Reasonable estimates of body segment slope and displacement were computed using cubic splines to describe anterior and posterior segments of the swimmer's body.

Experimental data was compared with simulated results from a numerical model of the prototype swimmer. Volterra series expansions based on measured swimmer kinematic parameters were computed for use in estimating caudal fin kinematic responses for different sets of tail plate motions. Results suggest that one may produce reasonable estimates of the swimmer's dynamics kinematic inputs. Either oversimplification of the overall model structure, or overestimates of the drag and added mass models appeared to cause a discrepancy between the simulated and actual values encountered by the prototype, leading to apparent low-pass characteristics in the model simulation.

6.2 Recommendations for Future Development

The framework developed in this thesis may be extended for use in a wide variety of applications including control system synthesis and experimental optimization of compliant biomimetic swimmers.

The range of swimming speeds was largely limited by the actuator's bandwidth. The use of a faster actuator should enable one to implement robust and powerful frequency domain identification methods, such as those described in [44], to produce a high-fidely model over a range of swimming speeds.

The limited speed of the existing prototype hinders the amount of hydrodynamic lift produced by the pectoral fins, which in turn limits the swimmer's potential three-dimensional capabilities. If a larger tank were made available, the swimmer's size could be increased, allowing for sufficient onboard battery storage, eliminating the need for the tether.

The vision system could be adapted to perform near real-time tracking of the swimmer. Following this line of thought, one could develop an adaptive algorithm that allowed the swimmer to learn how to swim and generate its own model based on experience.

A robust control scheme could be developed to enable trajectory tracking amidst flow disturbances or while retrieving payloads. Alternatively, a biomimetic behaviour-based control scheme could be designed based on actual fish behavioural responses to their inherently stochastic natural environment.

Appendix A

Camera Calibration

The calibration procedure utilizes MATLAB®routines written by Jean-Yves Bouguet [7]. The "Plumb Bob" distortion model is used, which assumes the form of a radial polynomial combined with a thin prism.

For a point $P = \begin{bmatrix} X_c & Y_c & Z_c \end{bmatrix}^\mathsf{T}$ in space with respect to the camera fixed frame Σ_c, we may write the normalized "pin hole" image projection as

$$x_n = \begin{bmatrix} X_c/Z_c \\ X_c/Z_c \end{bmatrix} = \begin{bmatrix} x \\ y \end{bmatrix} \tag{A.1}$$

The square of the radial position of a given projected point is then $r^2 = x^2 + y^2$.

The normalized distorted projection of P on the image plane is given by

$$x_d = \begin{bmatrix} x_{d_1} \\ x_{d_2} \end{bmatrix} = \left(1 + k_{c_1} r^2 + k_{c_2} r^4 + k_{c_5} r^6\right) x_n + dx \tag{A.2}$$

where

$$dx = \begin{bmatrix} 2k_{c_3} xy + k_{c_4} \left(r^2 + 2x^2\right) \\ k_{c_3} \left(r^2 + 2y^2\right) + 2k_{c_4} xy \end{bmatrix} \tag{A.3}$$

is the tangential distortion vector. The parameters k_c are the distortion coefficients and account for both radial and tangential distortion effects.

The pixel coordinates of x_d on the image plane are given by

$$\begin{bmatrix} x_p \\ y_p \end{bmatrix} = \begin{bmatrix} f_{c_1} \left(x_{d_1} + \alpha_c x_{d_2}\right) + c_{c_1} \\ f_{c_1} x_{d_2} + c_{c_2} \end{bmatrix} \tag{A.4}$$

where α_c is the skew angle accounting for the x- and y-pixel axes not being orthogonal to one another, and $f_{c_{1,2}}$ are the focal length coordinates in pixels. For square CCD pixels, the aspect ratio f_{c_2}/f_{c_1} should be unity.

Equation (A.4) may be rewritten as the following linear matrix equation

$$\begin{bmatrix} x_p \\ y_p \\ 1 \end{bmatrix} = \mathbf{K} \begin{bmatrix} x_{d_1} \\ x_{d_2} \end{bmatrix} \tag{A.5}$$

By comparing known pattern distances in many images with their physically measured lengths, regression routines are able to back-out the parameters making up

the matrix $\mathbf{K}$, which may then be used to "reverse" the optical distortion effects in acquired images.

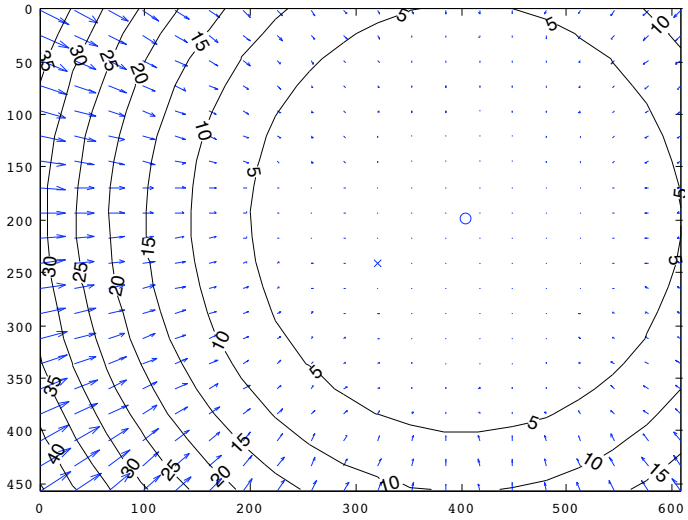

Figure A-1: Radial component of the camera optical distortion model.

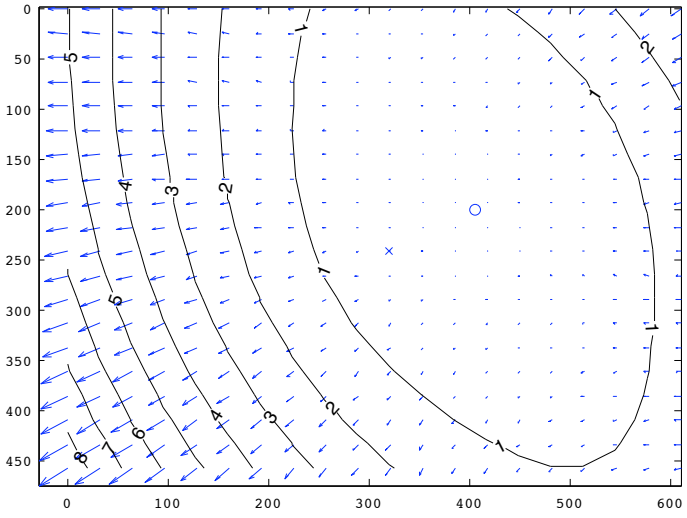

Figure A-2: Tangential component of the camera optical distortion model.

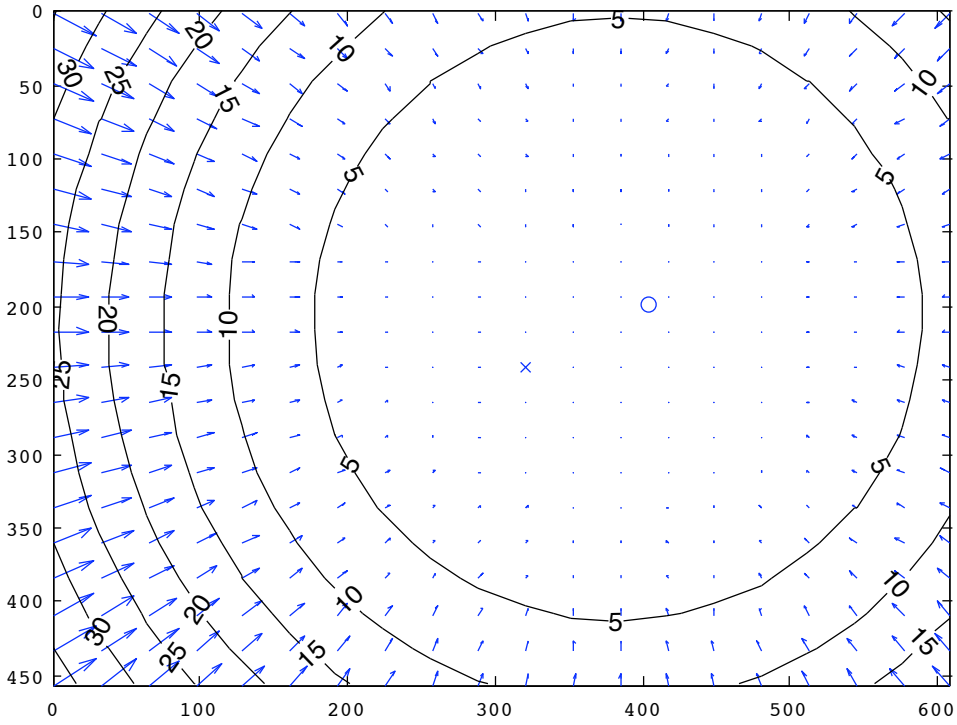

Figure A-3: Complete camera optical distortion model.

Parameter	Estimated value	Error bounds
Pixel error	$(0.3853, 0.2729)$	
Focal length	$(865.005, 857.146)$	$\pm\,(19.17, 16.05)$
Principal point	$(403.856, 198.571)$	$\pm\,(24.98, 29.34)$
Skew	0	± 0
Radial coefficients	$(-0.4651, 0.5075, 0)$	$\pm\,(0.06982, 0.3996, 0)$
Tangential coefficients	$(0.004789, 0.009708)$	$\pm\,(0.007208, 0.004747)$

Table A.1: Camera calibration parameters.

Appendix B

Materials

Part	Model Number	Manufacturer	Website
Air bearings	S205001	New Way®	unibrain.com
Camera	Fire-i™ Digital Board Camera	Unibrain®	unibrain.com
Dolly Rail	3030	80/20®	8020.net
Lens	2046	Unibrain®	unibrain.com
Marker IR LEDs	VSMG2700	Vishay®	vishay.com
Microcontroller	Make Controller	MakingThings	makingthings.com
Pec.toral fin servos	S3110	Futaba®	futaba.com
Silicone rubber	Ecoflex 00-10	Smooth-On®	smooth-on.com
Tail servo	HSR-5995TG	Hitec®	hitecrcd.com

Table B.1: Materials and parts.

Bibliography

[1] J. D. Anderson. Fundamentals of Aerodynamics. McGraw-Hill, 3rd edition, January 2001. 3.5.2, 3.6.3

[2] J. M. Anderson and N. K. Chhabra. Maneuvering and stability performance of a robotic tuna. Integrative and Comparitive Biology, 42(1):118–126, February 2002. 2.3

[3] J. M. Anderson and P. A. Kerrebrock. The vorticity control unmanned undersea vehicle (vcuuv): An autonomous robot tuna. Technical report, Draper Labs, 2000. 2.3

[4] D. Barrett, M. Grosenbaugh, and M. Triantafyllou. The optimal control of a flexible hull robotic undersea vehicle propelled by an oscillating foil. Proceedings of the 1996 Symposium on Autonomous Underwater Vehicle Technology, pages 1–9, 1996. 2.3

[5] D. S. Barrett. The design of a flexible hull undersea vehicle propelled by an oscillating foil. Master's thesis, Massachusetts Institute of Technology, 1994. 2.3

[6] D. Bernal, J. M. Donley, R. E. Shadwick, and D. A. Syme. Mammal-like muscles power swimming in a cold-water shark. Nature, 437:1349–1352, October 2005. 2.2, 4-10

[7] J.-Y. Bouguet. Camera calibration toolbox for matlab. In http://www.vision.caltech.edu/bouguetj/. World Wide Web electronic publication, June 2008. A

[8] Campagno. FAO Species Catalogue: Sharks of the World, volume 4. Food and Agriculture Organization, 1984. 3.4, 3.6.1

[9] J.-Y. Cheng and R. Blickhan. Bending moment distribution along swimming fish. J. Theor. Biol., 168(3):337–348, 1994. 2.2

[10] J.-Y. Cheng, T. J. Pedley, and J. D. Altringham. A contiuous dynamic beam model for swimming fish. Philosophical Transactions: Biological Sciences, 353(1371):981–997, June 1998. 2.2

[11] J.-Y. Cheng, L.-X. Zhuang, and B.-G. Tong. Analysis of swimming three-dimensional waving plates. Journal of Fluid Mechanics, 232:341–355, 1991. 2.2

[12] J. E. Colgate and K. M. Lynch. Mechanics and control of swimming: a review. Oceanic Engineering, IEEE Journal of, 29(3):660–673, July 2004. 2.2

[13] B. Etkin and L. D. Reid. Dynamics of Flight: Stability and Control. Wiley, 3rd edition, 1996. 1.1

[14] L. Ferry and G. V. Lauder. Heterocercal tail function in leopard sharks: a three-dimensional kinematic analysis of two models. Journal of Experimental Biology, 199(10):2253–2268, 1996. 2.2, 3.5.2, 3.6.1

[15] F. E. Fish and L. E. Shannahan. The role of the pectoral fins in body trim of sharks. Journal of Fish Biology, 56(5):1062–1073, May 2000. 2.2, 3.5.2

[16] R. Froese and D. Pauly. Fishbase. In http://www.fishbase.org. World Wide Web electronic publication, June 2008. (document), 3-6

[17] S. F. Hoerner. Fluid-Dynamic Drag: Practical information on aerodynamic drag and hydrodynamic resistance. Hoerner Fluid Dynamics, Bakersfield, CA, 2 edition, 1992. 3.5.3

[18] H. Hu, J. Liu, I. Dukes, and G. Francis. Design of 3d swim patterns for autonomous robotic fish. IEEE/RSJ International Conference on Intelligent Robots and Systems, pages 2406–2411, 2006. 2.3

[19] V. Klein and E. A. Morelli. Aircraft System Identification: Theory and Practice. AIAA, 2006. 5.1

[20] M. Korenberg and I. Hunter. The identification of nonlinear biological systems: Volterra kernel approaches. Annals of Biomedical Engineering, 24(4):A250–A268, 1996. 5.3

[21] G. V. Lauder. Function of the caudal fin during locomotion in fishes: Kinematics, flow visualization, and evolutionary patterns. Amer. Zool., 40:101–122, 2000. 2.2, 2.2

[22] G. V. Lauder and E. G. Drucker. Morphology and experimental hydrodynamics of fish fin control surfaces. Oceanic Engineering, IEEE Journal of, 29(3):556–571, 2004. 2.2

[23] M. J. Lighthill. Note on the swimming of slender fish. Journal of Fluid Mechanics, 9, 1960. 2.2, 3.2

[24] M. J. Lighthill. Hydromechanics of aquatic animal propulsion. Annual Reviews of Fluid Mechanics, 1:413–446, 1969. 2.2

[25] M. J. Lighthill. Aquatic animal propulsion of high hydromechanical efficiency. Journal of Fluid Mechanics, 44(2):265–301, 1970. 2.2

[26] M. J. Lighthill. Large-amplitude elongated-body theory of fish locomotion. Proceedings of the Royal Society of London. Series B, Biological Sciences, 179(1055):125–138, November 1971. 2.2

[27] R. L. McMasters, C. P. Grey, J. M. Sollock, R. Mukherjee, Andre Benard, and A. R. Diaz. Comparing the mathematical models of lighthill to the performance of a biomimetic fish. Bioinspiration & Biomimetics, 3(1), 2008. 2.2

[28] K. A. Morgansen, T. M. La Fond, and J. X. Zhang. Agile maneuvering for fin-actuated underwater vehicles. In Proceedings of the 2006 Second International Symposium on Communicatons, Control and Signal Processing, 2006. 2.3, 3.7

[29] K. A. Morgansen, B. I. Triplett, and D. J. Klein. Geometric methods for modeling and control of free-swimming fin-actuated underwater vehicles. IEEE Transactions on Robotics, 2007. 2.3, 3.7

[30] U. K. Muller, BLE. Van Den Heuvel, E. J. Stamhuis, and J. J. Videler. Fish foot prints: morphology and energetics of the wake behind a continuously swimming mullet (chelon labrosus risso). Journal of Experimental Biology, 200(22):2893–2906, 1997. 2.2, 2-4

[31] J. N. Newman. Marine Hydrodynamics. MIT Press, 1977. 1.1, 3.5.1

[32] J. N. Newman and T.Y. Wu. A generalized slender-body theory for fish-like forms. Journal of Fluid Mechanics, 57(4):673–693, 1973. 1.1

[33] N. Otsu. A threshold selection method from gray-level histograms. Systems, Man and Cybernetics, IEEE Transactions on, 9(1):62–66, 1979. 5.1

[34] M. Raffel, C. Willert, S. Wereley, and J. Kompenhans. Particle Image Velocimetry: A Practical Guide. Springer, 2 edition, 2007. 2.2

[35] D. A. Read, F. S. Hover, and M. S. Triantafyllou. Forces on oscillating foils for propulsion and maneuvering. Journal of Fluids and Structures, 17(1):163–183, 2003. 2.3, 2-5, 3.6.2, 3.6.2

[36] M. B. Read. Performance of biologically inspired flapping foils. Master's thesis, Massachusetts Institute of Technology, 2006. 2.3, 3.6.2

[37] L. Schouveiler, F. S. Hover, and M. S. Triantafyllou. Performance of flapping foil propulsion. Journal of Fluids and Structures, 20(7):949–959, October 2005. 2.3

[38] Science Museum Science and Society Picture Library. Robotuna, c 2000. In http://www.sciencemuseum.org.uk. World Wide Web electronic publication, 2000. 2-6

[39] M. Sfakiotakis, D. M. Lane, and J. B. C. Davies. Review of fish swimming modes for aquatic locomotion. IEEE Journal of Oceanic Engineering, 24(2):237–252, 1999. 2.1.2, 2-3, 2.2, 3.6.2

[40] J. A. Sparenberg. Survey of the mathematical theory of fish locomotion. Journal of Engineering Mathematics, 44(4):395–448, 2002. 1.1, 2.2

[41] R. F. Stengel. Flight Dynamics. Princeton University Press, 41 William Street, Princeton, New Jersey 08540, 1st ed. edition, 2004. 1.1

[42] K. Streitlien, G. S. Triantafyllou, and M. S. Triantafyllou. Efficient foil propulsion through vortex control. AIAA Journal, 34(11):2315–2319, 1996. 2.3

[43] G. Taylor. Analysis of the swimming of long and narrow animals. Proceedings of the Royal Society of London. Series A, Mathematical and Physical Sciences, 214(1117):158–183, August 1952. 2.2

[44] M. B. Tischler and R. K. Remple. Aircraft and Rotorcraft System Identification. AIAA, 1st ed. edition, 2006. 6.2

[45] M. S. Triantafyllou, A. H. Techet, and F. S. Hover. Review of experimental work in biomimetic foils. IEEE Journal of Oceanic Engineering, 29(3):585–594, July 2004. 2.3

[46] M. S. Triantafyllou and G. S. Triantafyllou. An efficient swimming machine. Scientific American, 272(3), 1995. 5.4

[47] P. Valdivia y Alvarado. Design of Biomimetic Compliant Devices For Locomotion in Liquid Environments. PhD thesis, Massachusetts Institute of Technology, 2007. 2.2, 2.3, 3, 3.3, 3.3, 3.3, 4.4.1, 5.4

[48] P. Valdivia y Alvarado and K. Youcef-Toumi. Performance of machines with flexible bodies designed for biomimetic locomotion in liquid environments. Proceedings of the 2005 IEEE International Conference on Robotics and Automation, pages 3324–3329, 2005. 2.3, 3.3

[49] P. Valdivia y Alvarado and K. Youcef-Toumi. Design of machines with compliant bodies for biomimetic locomotion in liquid environments. Journal of Dynamic Systems, Measurement, and Control, 128(1):3–13, 2006. 2.3, 3.3, 4.4.1

[50] J. J. Videler. Fish Swimming. Fish and Fisheries Series 10. Chapman and Hall, 1st ed. edition, July 1993. 1.1, 2.2, 2.2, 5.2.2

[51] W. Vorus. Swimming of the semi-infinite strip revisited. Journal of Engineering Mathematics, 51(1):35–55, 2005. 2.2

[52] C. D. Wilga and G. V. Lauder. Three-dimensional kinematics and wake structure of the pectoral fins during locomotion in leopard sharks triakis semifasciata. J Exp Biol, 203(15):2261–2278, 2000. 2-2, 2.2, 3.5.2

[53] C. D. Wilga and G. V. Lauder. Functional morphology of the pectoral fins in bamboo sharks, chiloscyllium plagiosum: Benthic vs. pelagic station-holding. Journal of Morphology, 249(3):195–209, 2001. 2.2, 3.5.2

[54] C. D. Wilga and G. V. Lauder. Function of the heterocercal tail in sharks: quantitative wake dynamics during steady horizontal swimming and vertical maneuvering. Journal of Experimental Biology, 205:2365–2374, 2002. 2.2, 3.6.1

[55] C. D. Wilga and G. V. Lauder. Biology of Sharks and Their Relatives, chapter Biomechanics of locomotion in sharks, rays, and chimeras, pages 139–164. CRC Press, 2004. 2.2, 3.7, 3-10

[56] M. I. Wolf. Open loop performance of a biomimetic flapping foil autonomous underwater vehicle. Master's thesis, Massachusetts Institute of Technology, 2006. 2.3

[57] T. Y. Wu. Mathematical biofluiddynamics and mechanophysiology of fish locomotion. Mathematical Methods in the Applied Sciences, 24(17–18):1541–1564, December 2001. 1.1

[58] Q. Zhu, M. J. Wolfgang, D. Yue, and M. S. Triantafyllou. Three-dimensional flow structures and vorticity control in fish-like swimming. Journal of Fluid Mechanics, 468:1–28, April 2002. 2.2